

Drag upon a sphere suspended in a low magnetic-Reynolds number MHD channel flow

Jules Delacroix

Electromagnetic Processing of Materials (EPM) Group, Materials and Processes Science and Engineering Laboratory (SIMaP), Grenoble Institute of Technology (Grenoble-INP)/Université Grenoble-Alpes/CNRS, 38402 Saint Martin d'Hères, France

and Laboratoire d'Etudes et d'Expérimentations pour les Accidents Graves (LEAG), CEA Cadarache, 13108 St-Paul-lez-Durance, France

Laurent Davoust*

Electromagnetic Processing of Materials (EPM) Group, Materials and Processes Science and Engineering Laboratory (SIMaP), Grenoble Institute of Technology (Grenoble-INP)/Université Grenoble-Alpes/CNRS, 38402 Saint Martin d'Hères, France



(Received 4 April 2018; published 5 December 2018)

A permanent magnetohydrodynamics (MHD) channel flow past a stationary sphere is investigated, with a static magnetic field transversally applied and no-slip conditions taken into account. The sphere is subject to laminar flow conditions with the Reynolds number ranging from the Stokes regime up to values corresponding to the inertial regime ($Re_p = 130$ at most for the particle Reynolds number). The maximum value of the Hartmann number is $Ha = 200$. After a brief review of the existing literature of three-dimensional (3-D) MHD flows past an obstacle, a 3-D numerical approach is developed, which is systematically compared to asymptotic predictions ($Ha = 0$, $Ha \rightarrow \infty$). Atypical flow patterns are made evident, especially characterized by the gradual emergence of Hunt's wake for a sufficiently large particle Stuart number N_p . Some original correlations are put forward for the wake length and the drag coefficient. Finally, an original scaling law highlighting the significant influence of the outer magnetic field on the transition between different MHD flow regimes is drawn up.

DOI: [10.1103/PhysRevFluids.3.123701](https://doi.org/10.1103/PhysRevFluids.3.123701)

I. INTRODUCTION

A. Context, objectives, and methodology proposed

The emergence of many industrial issues related to heterogeneous electroconductive flows has brought magnetohydrodynamics (MHD) flows in the presence of an obstacle or a dispersed phase to center stage. For instance, the use of a mechanical obstacle, the use of an electrical obstacle, or a combination thereof may turn out to be a means of heat transfer enhancement [1]. When use is made of MHD in microfluidic devices for the purpose of performing (immuno)magnetic cell separation or magnetic-activated cell sorting [2], the conducting fluid often contains insulating inclusions or bubbles. In metallurgical processes, molten metal may be heated and stirred by induction, with additional stirring performed through gas bubbling [3]. In a long-term view, the use of liquid metals for cooling magnetically confined fusion reactors offers many potential advantages, such as higher heat transfer performance, higher boiling temperature than conventional liquids, and tritium

*Corresponding author: laurent.davoust@simap.grenoble-inp.fr

breeding in the coolant if lithium-lead alloys are used [4]. However, the interplay between the liquid metal motion and the strong magnetic fields generated by the magnetic confinement leads to a MHD flow inside liquid Li/Pb. As often mentioned in the literature [5], depending on the direction of the magnetic field relative to the normal unit vector at the cooling walls, convective heat transfers can be severely affected. Heat transfer enhancement strategies are currently developed in order to comply with the two-dimensional (2-D) tendency of MHD flows, based on electrically driven vortices [6] or the insertion of obstacles [7], for instance. An alternative strategy based on the generation of (small) gas bubbles in the blanket has been proposed, either by boiling [8] or bubbling [9]. For the latter strategy, the purpose consists of lowering the MHD pressure drop by reducing the apparent electrical conductivity of the fluid.¹

As a consequence of the previous considerations, the behavior of gas bubbles or spherical inclusions suspended in electroconductive fluids that are subjected to external magnetic fields stands as an issue of prime interest. It should be noted that although insulating inclusions such as gas bubbles do not experience a magnetic force directly, they can be submitted to a MHD-induced buoyancy force. The scientific literature on this topic covers a wide range of dispersed MHD flow layouts, ranging from “collective” configurations to single bubble dynamics. The former class involves bubble plumes subjected to dc magnetic fields either transverse to the main flow direction [11] or streamwise [12,13]. With respect to gas bubble or spherical inclusions in MHD flows, the available literature becomes more scarce, focusing on paths, wakes, and even shapes of bubbles under the influence of aligned or transverse dc fields. The reader is free to refer to direct numerical simulations [14–17] or to ultrasonic Doppler velocimetry measurements of terminal velocities and wake structures [18]. Surprisingly enough, despite the fundamental features of the MHD flow past a sphere or a bubble, it seems to the best of our knowledge that the available literature still remains incomplete. As shown hereafter in Sec. I C 3, the rare available studies do not really take the influence of confinement into account, especially when the magnetic field is transversally applied with respect to the main flow. This approach could be justified in the case of purely hydrodynamic flows, provided that the boundaries are far enough from the inclusion. However, in the presence of a transverse magnetic field, due to the importance of the electric circuit and the outstanding properties of the Hartmann layers, the role of the side walls turns out to be decisive whatever the typical size of the system under consideration. Besides, the few existing works to be considered correspond to asymptotic conditions of a MHD flow past a cylindrical obstacle, i.e., where the outer magnetic field is sufficiently strong for the quasi-two-dimensional approximation to be valid (known as the Sommeria and Moreau [SM82] approximation [1,19]). When use is made of the SM82 approximation, the obstacle must extend all along the magnetic field direction with no symmetry breakup [20,21]. As a consequence, it seems that most of the obstacles considered in the literature never resemble a sphere, with the notable exception of the reference analytical article by Hunt and Ludford [22], whose most salient features are introduced in Sec. I C 3, and hereafter referred to as the HL68 model.

Concerning the meaningful case of the MHD duct flow past a sphere beyond the SM82 approximation, it seems that the works of Haverkort and Peeters [3,23] are the only investigations available. However, as shown hereafter, the previous authors implement free-slip conditions at boundaries. Despite the induced simplifications in term of numerical resources, this results in a major difference with respect to the more realistic no-slip boundary conditions. Indeed, Hartmann layers cannot be generated without velocity gradients in the vicinity of duct walls whose orientation is orthogonal to the outer field. Consequently, even the works of Haverkort and Peeters do not address the critical issue linked to the role played by duct walls. Given the outstanding role played

¹Obviously, even if the generation of bubbly MHD flows inside the blanket could contribute to a better convective heat transfer, the injection of a gaseous phase degrades the conductive part of heat removal by reducing the apparent thermal conductivity. A tradeoff must be found between the latter phenomena, with the ultimate aim to enhance the Nusselt number [10].

by these Hartmann layers and their strong impact on MHD flow whatever the distance to the obstacle [22,24], it appears (to the best of our knowledge) that there remains a deficit in the literature.

The first goal of this paper is therefore to extend the work of Haverkort and Peeters to the insightful case of a rigid (insulating) sphere suspended into a MHD flow, confined within electrically insulated motionless walls, with special emphasis on the role played by the Hartmann layers.

Moreover, as exposed hereafter in Sec. IC, most of related analytical studies focus on asymptotic regimes of the MHD sphere problem, assuming that the governing dimensionless numbers (Re , Ha , N , and their particulate counterparts, indexed p , all defined below) are either asymptotically small or asymptotically large. Note also that the numerical results of Haverkort and Peeters are restricted to ($Re_p \leq 100$, $Ha_p \leq 20$). Consequently, beyond the purpose of highlighting the physical mechanisms and original flow patterns linked to the sphere MHD problem, another goal is to extrapolate the existing asymptotic results to unknown parameter regimes. In this study, we consider the ranges $0.6 \leq Re_p \leq 129$, $0 \leq Ha \leq 200$, and $0 \leq N \leq 1.67 \times 10^4$. The maximum value for the Reynolds number corresponds to the threshold of hydrodynamic instabilities (not included here), while the maximum value for the Hartmann number ensures the proper meshing of the Hartmann layers without prohibitive computing time costs.

The following methodology is proposed. First of all, a physical modeling of the sphere MHD problem is proposed, including geometry, additional assumptions, governing equations, and boundary conditions. In the present paper, the implementation of a 3-D numerical approach is favored, which is justified by the symmetry breakup in the physical layout (see Fig. 8) as well as by the necessity to describe nonasymptotic regimes. Classically, the finite-element method (FEM) is used to discretize Maxwell equations in electromagnetism. However, this is not always the case in fluid mechanics, as, contrary to the finite-volume method (FVM), the discrete approximation is *a priori* not conservative. Consequently, if the FEM is chosen to tackle a MHD problem, as we do, particular care is required to ensure a conservative solution. Therefore, numerical modeling is systematically benchmarked with the reference results exposed in Sec. IC, first in the purely hydrodynamic case ($Ha = 0$). Then, once this benchmarking case secured, the outer magnetic field is added, and the numerical results are benchmarked with either Hunt and Ludford's (HL68) model ($Ha, N \gg 1$) or with Haverkort and Peeter's results ($Re_p \leq 100$, $Ha_p \leq 20$). Eventually, these results are extrapolated to unknown MHD flow regimes, and the most salient flow patterns are discussed. New correlations for the flow coefficients are also proposed, along with a scaling law emphasizing the influence of the outer magnetic field on the transition between different flow regimes.

Thus, the laminar permanent MHD duct flow past an insulating sphere is systematically investigated in this paper, taking confinement effects into account, for all magnitudes of the magnetic and velocity fields, up to (but not including) the threshold of hydrodynamic-hydrodynamic instabilities. The SM82 approximation is not considered so that the flow is considered fully three dimensional (3-D).

Prior to any investigation of our own, the flow coefficients characterizing a (magneto)hydrodynamic flow past an obstacle are defined. Then, the main physical issues related to the MHD flow past a sphere are highlighted, allowing us to clarify the typical flow configuration under consideration. The state of the art is carefully reviewed, given the fundamental aspect of underlying issues. Eventually, this detailed review allows us to define properly the scope of this paper. Finally, the 3-D calculations presented herein are also applicable for a levitating (non-neutrally-buoyant) sphere located on the axis of a channel with a square cross section. Although the sphere considered is fixed with respect to the channel walls, the present study is a first step, typical of the literature of two-phase flows with no consideration for the sliding velocity (flotation processes, flowmeters with float).

B. Notations and flow coefficients

The system under consideration consists of an immersed spherical body whose typical size is d , suspended in an electroconductive fluid flow, as displayed Fig. 1. The flow is confined between duct walls, whose typical transverse length is L , and the control volume under consideration includes

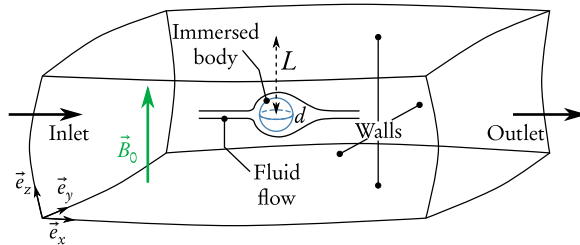


FIG. 1. Overall layout of the MHD sphere problem.

the obstacle, with an inlet and an outlet boundary condition. The flow can be subjected to an outer magnetic field \vec{B}_0 , directed along the transverse direction with respect to the main flow (see Appendix A for further discussion about the latter choice).

First of all, a set of flow coefficients is classically defined in order to characterize the hydrodynamic flow past an immersed body, beginning with the dimensionless number governing the flow patterns in the vicinity of the inclusion, i.e. the particle Reynolds number Re_p . It classically governs the interplay between inertial and viscous effects and can be defined as follows:

$$\text{Re}_p = \frac{\rho V d}{\eta}, \quad (1)$$

where ρ and η are density and dynamic viscosity of the surrounding fluid, d is the typical size of the body, and V is a typical flow velocity (often defined as the typical relative velocity between the body and the surrounding fluid). If the suspending flow is confined within duct walls, a (bulk) Reynolds number can also be introduced:

$$\text{Re} = \frac{\rho V L}{\eta}. \quad (2)$$

The body is subjected to a force \vec{F} , exerted by the surrounding flow, due to both pressure (denoted p) and viscous forces, the latter being linked to fluid viscosity (η) and velocity (denoted \vec{v}) gradients. The streamwise projection of this hydrodynamic force is called the drag force, while the transverse projection is called the lift force. In this paper, the lift force is neglected for symmetry reasons. If the fluid far from the obstacle flows along the \vec{e}_x direction, the drag force is generally defined as

$$\vec{F}_d = (\vec{F} \cdot \vec{e}_x) \vec{e}_x = \left(\iint_S (\mathbb{T} \cdot \vec{e}_r) \cdot \vec{e}_x \right) dS \vec{e}_x, \quad (3)$$

where \mathbb{T} is the mechanical stress tensor, S is the surface of the sphere, and \vec{e}_r is the outer normal to this surface (see Fig. 2). For instance, in the case of an axisymmetric flow past a spherical inclusion, Eq. (3) is

$$\vec{F}_d = F_d \vec{e}_x = \int_0^\pi 2\pi R^2 \sin(\theta) T_{rx}(R, \theta) d\theta \vec{e}_x, \quad (4)$$

r and θ are the spherical coordinates attached to the sphere, $R = d/2$ is the sphere radius, and T_{rx} is the projection of the mechanical stress tensor defined as

$$T_{rx} = T_{r\theta} \cos(\theta) + T_{rr} \sin(\theta), \quad (5)$$

$$T_{rr} = -p + 2\eta \frac{\partial v_r}{\partial r}, \quad T_{r\theta} = \eta \left(r \frac{\partial \left(\frac{v_\theta}{r} \right)}{\partial r} + \frac{1}{r} \frac{\partial v_r}{\partial \theta} \right). \quad (6)$$

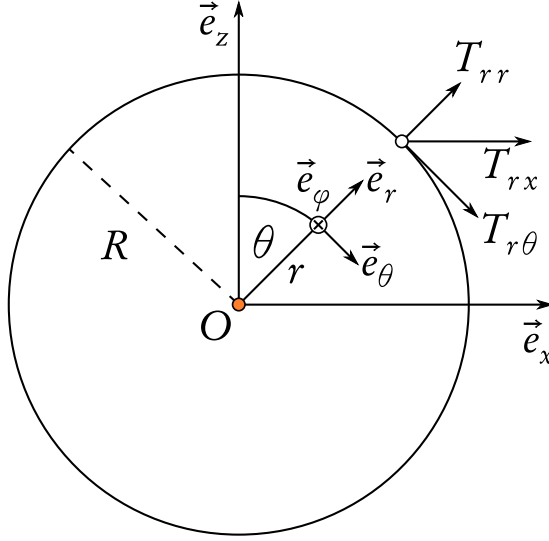


FIG. 2. Projection of the mechanical stress tensor leading to the definition of the drag force.

In practice, the dimensionless group related to the drag force is preferentially used. This dimensionless coefficient is called the drag coefficient, and is defined as follows:

$$C_d = \frac{|F_d|}{\frac{1}{2}\rho V^2 \pi R^2}. \quad (7)$$

The drag coefficient is particularly used to benchmark the numerical calculations performed in Sec. III (see also Appendix B).

An additional flow coefficient can be defined for characterizing flow recirculation areas at higher Re_p values. This parameter is the length of the steady recirculation area, denoted L_w , measured between the rear point of the obstacle and the tail of the recirculation region. Typically, the change of sign of the velocity along the center line behind the sphere (in the main flow direction, or streamwise) gives access to this length. Note that the influence of confinement due to the presence of duct walls is discussed in Sec. IC 1.

When an outer dc field is added, eddy currents are induced in the electroconductive fluid in motion. These currents interact with the external field to generate the Lorentz force, which may compete with other hydrodynamic phenomena. Two dimensionless numbers can be defined to describe this interplay. In the case of a confined (i.e., duct) flow, at duct scale L , they are called the (bulk) Hartmann number Ha and the Stuart number N :

$$Ha = B_0 L \sqrt{\frac{\sigma}{\eta}}, \quad N = \frac{Ha^2}{Re} = \frac{\sigma B_0^2 L}{\rho V}, \quad (8)$$

where B_0 is the typical intensity of the outer magnetic field and σ is the electrical conductivity of the surrounding fluid. Ha governs the balance between electromagnetic and viscous effects, while N governs the balance between electromagnetic and inertial effects [5]. At particle scale d , the particle Hartmann number Ha_p and Stuart number N_p can be defined as

$$Ha_p = B_0 d \sqrt{\frac{\sigma}{\eta}}, \quad N_p = \frac{Ha_p^2}{Re_p} = \frac{\sigma B_0^2 d}{\rho V}. \quad (9)$$

The qualitative definition of the other flow coefficients previously introduced (wake length and drag coefficient) remains unchanged, though the outer magnetic field actually affects their values (Sec. IC 3). Subsequently, both particle [Eqs. (1) and (9)] and bulk [Eqs. (2) and (8)] dimensionless numbers are used in this paper.

C. State of the art

The focus is first set upon the typical patterns linked to the hydrodynamic flow past a rigid sphere, in the case where no outer magnetic field is present. Some insightful MHD features are then introduced, emphasizing the influence of the Hartmann layers on the flow topology. For the readers familiar with MHD or multiphase flows concepts, some of the following ingredients can be easily skipped.

1. Hydrodynamic flow regimes ($B_0 = 0$)

Depending on the value of the particle Reynolds number, a first distinction can be made between two flow regimes. On the one hand, when Re_p is low (typically $Re_p < 1$), the creeping flow regime can be considered. On the other hand, for intermediate values ($1 < Re_p < 130$), the steady wake regime gradually intensifies, with the generation of recirculation regions at the rear of the obstacle. In the latter case, inertial effects must be taken into account, leading to the flow separation and to the appearance of two steady recirculation regions, valid up to $Re_{p,max} = 130$ (see, e.g., Clift *et al.* [25]). Flow patterns are investigated through the flow coefficients previously introduced.

The generation of new flow patterns with Re_p can be divided into two steps. The first interval $1 < Re_p < 20$ corresponds to an unseparated flow regime. The flow still sticks to the whole sphere surface, and no separation is visible. Asymmetry becomes more marked. At the onset value $Re_p = 20$, flow separation occurs at the rear stagnation point and vortical patterns arise. Finally, as Re_p increases beyond 20, the recirculation regions appear. These regions are symmetric with respect to the wake centerline; they develop at the rear of the sphere and are found to lengthen downstream.

The extent of the steady recirculation area can be described by means of the parameter L_w . When focusing on the data for which $Re_p < 130$, the following correlation can be derived from data collected in Ref. [25]:

$$\frac{L_{w,sphere}}{d} = c_1(Re_p) = \frac{2747}{5000} \ln(Re_p) - \frac{8347}{5000} \quad \text{for } Re_p \leq 100. \quad (10)$$

Now, with respect to the drag coefficient, the following piecewise correlation is proposed [25], which encompasses a large set of experimental data:

$$C_{d,Clift,s} = c_2(Re_p) = \begin{cases} \frac{24}{Re_p} \left(1 + \frac{263}{2000} Re_p^{\frac{41}{50} - \frac{1}{20} \log_{10}(Re_p)} \right) & \text{if } Re_p \leq 20, \\ \frac{24}{Re_p} \left(1 + \frac{387}{2000} Re_p^{\frac{1261}{3000}} \right) & \text{if } Re_p \in]20, 130]. \end{cases} \quad (11)$$

2. Impact of flow confinement ($B_0 = 0$)

Up to now, the flow domain has been considered unbounded, so that the typical velocity of the flow far from the inclusion has been considered uniform. In nonacademic situations, the flow domain is bounded by walls, separated by a $2L$ distance. Now, depending on the value of the *blockage ratio*, $\lambda = \frac{d}{2L}$, the confinement may alter the flow patterns past the spherical inclusion.

Let us consider a self-established channel flow. At the inlet, the hydrodynamic velocity profile is imposed according to a parabolic Poiseuille velocity profile. The typical velocity V corresponds now to the maximum velocity reached at the inlet, i.e., at the channel centerline. Moreover, the flow between the sphere and the duct walls is locally accelerated, in link with mass conservation. Finally, the walls can also interfere with the wake released by the obstacle. From a quantitative point of view, the joint presence of the side walls and the sphere generates an additional pressure gradient along the transverse direction and viscous dissipation enhancement at the duct walls. Even if they leave the transitional Re_p value between the two flow regimes quite unchanged (for moderate λ values, typically up to $\lambda = 0.2$), these two combined effects are suspected to impact the values of the two other flow coefficients, beginning with the length of the recirculation area L_w , for the steady wake regime. An increase of λ causes a shortening of the steady recirculation region, and thus a decrease of L_w , at a given Re_p . For instance, for $\lambda = 0.125$, L_w differs within 5–10% from its value for the $\lambda = 0$ (unbounded) case [26].

Now, with respect to the drag coefficient, the difference with the unbounded configuration can be more significant. Indeed, for $\lambda = 0.125$, C_d can reach values up to 35% higher than in the unbounded case, as shown by Wham *et al.* [27]. These authors propose a new correlation for drag as a function of both Re_p and λ , valid for $\text{Re}_p < 130$, $\lambda \in [0.08, 0.7]$:

$$C_{d,\text{Wham}} = c_3(\text{Re}_p) = \frac{\left[1 + \frac{927}{25000} \left(\frac{\text{Re}_p}{2}\right)^{\frac{757}{500} - \frac{127}{1250} \ln\left(\frac{\text{Re}_p}{2}\right)}\right] \left(1 - \frac{12901}{17007} \lambda^5\right)}{1 - \frac{1657}{2500} \lambda - \frac{729}{500} e^{-\frac{1127}{20000} \left(\frac{\text{Re}_p}{2}\right)} + \frac{4173}{2000} \lambda^3 - \frac{4267}{2500} \lambda^5 + \frac{72603}{100000} \lambda^6 \text{Re}_p} \cdot 24. \quad (12)$$

3. Impact of a transverse magnetic field: A brief review

The influence of an outer transverse dc field upon electroconductive flows past obstacles of various shapes is briefly reviewed, including obstacles such as gaseous (nonrigid) bubbles. The literature about MHD flows past obstacles is indeed reduced, and only scarce information could be given if focus is put only on spherical bodies.

The addition of an external dc magnetic field can significantly alter the core flow topology, regardless of the presence of the body. In the case of an electroconductive channel flow with insulating walls normal to a transverse dc field, the Hartmann layers exert an active control over the core flow, leading to a typical velocity V proportional to $O(1/\text{Ha})$ in the core region. The active control is associated to the fact that the order of magnitude of the core-flow velocity is directly controlled by the electric current density closing within the Hartmann layers [5]. The presence of an obstacle is also expected to alter deeply the topology of the MHD core flow, because Hartmann layers may develop along the surface of the inclusion, causing a complete alteration of the electric circuit. Conversely, because the surrounding electroconductive liquid is affected by Lorentz forces, immersed insulating objects can experience noticeable MHD effects by way of the drag coefficient. Thus, the interplay between the immersed body and bulk dynamics is likely to generate particularly original flow patterns.

In the literature, there are few existing theoretical works describing the MHD of an electroconductive flow past a rigid sphere subjected to an outer transverse dc field, essentially because of the complexity of the mathematical model, even at low magnetic Reynolds number $\text{Rm} = \mu\sigma VL$, where μ is the magnetic permeability of the medium under consideration. Nonetheless, there is a certain amount of numerical and experimental data, for both streamwise and transverse magnetic fields. As already explained (see, e.g., Appendix A), the streamwise orientation of the outer field is left aside from the analysis (see Refs. [12,15,18,28] for a nonexhaustive list of references). The most significant achievements concerning the transverse layout are now highlighted, beginning with the few existing analytical results for asymptotic values of Re (Re_p), Ha (Ha_p), and N (N_p).

Among the rare papers investigating MHD channel flows past an obstacle, the pioneering one by Hunt and Ludford [22] is entirely based on matched asymptotic calculations. Its most insightful results are clarified later in MHD textbooks (see, e.g., Ref. [5]). The 3-D MHD flow past an obstacle of arbitrary shape² is considered by HL68 in the asymptotic case: $N \gg 1$, $\text{Ha} \gg 1$. The obstacle is suspended in an electroconductive flow, confined within duct walls with typical extent L along \vec{e}_y (corresponding to half the height of the duct), and unbounded along \vec{e}_x and \vec{e}_z . The flow reaches a typical (maximum) velocity V far from the obstacle and is subjected to an external dc magnetic field $\vec{B}_0 = B_0 \vec{e}_y$. The typical geometry is displayed in Fig. 3.

Within the assumption $N, \text{Ha} \gg 1$ (which only implies $\text{Ha}^2 \gg \text{Re}$, Re being potentially large), some original features appear. The flow is indeed structured into two main regions, where the velocity and the electric current density gradients are weak: a column C , whose axis is aligned with \vec{B}_0 , circumscribing the sphere, and the region E external to this column. The gradients of \vec{v} and \vec{j} are actually located in thin layers: the Hartmann layer between the obstacle and the column C , denoted HS , the (classical) Hartmann layers located near the duct walls, called HW , and an intermediate

²Here, we shall restrict our attention to a spherical body.

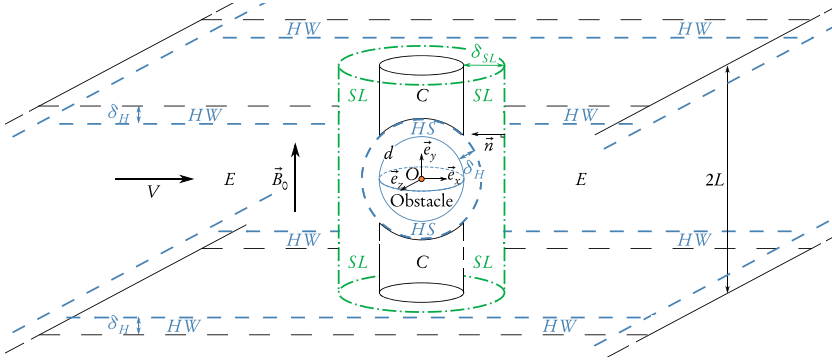


FIG. 3. Different regions of the MHD flow (not to scale) around a sphere when $Ha, N \gg 1$, according to the (matched asymptotic) HL68 model.

region SL constituting a Shercliff layer between C and E . The Hartmann layers exhibit a typical thickness $\delta_H^* = 1/Ha$, while the Shercliff layer is $\delta_{SL}^* = 1/\sqrt{Ha}$ thick. As highlighted in Fig. 3, the areas C and E constitute the internal and external core-flow regions, respectively. They are deeply influenced by the different boundary layers and are of primary interest in view of analyzing the impact of the spherical obstacle on the bulk MHD flow. In these areas, viscosity effects are negligible. Performing a matched asymptotic expansion based on $Ha, Re \gg 1$, the authors prove that the flow in the region E is curl free (because of the Hartmann layers HW), while the column C remains motionless, and current free. Henceforth, the latter is referred to as Hunt’s wake, adopting recent terminology [24,29].

An overview of the most significant results is proposed in Fig. 4. As shown in Fig. 4(a), the velocity field in the external core region E is analogous to the electric field in vacuum around a perfectly conducting cylinder. The streamlines penetrate into the column perpendicularly to its boundary but circulate around the internal core C to concentrate in the shear layer, where a large azimuthal component $v_\zeta^* = O(\delta_{SL}^*)$ appears [Fig. 4(b)]. In this layer, the electric current streamlines

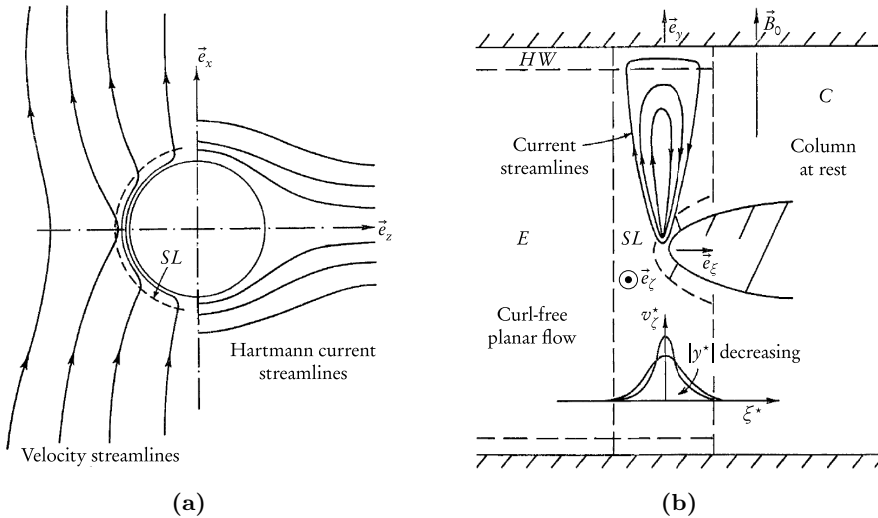


FIG. 4. Typical flow patterns past a spherical obstacle when $Ha, N \gg 1$ [22]. (a) Streamlines and current lines for flow over a nonconducting sphere; (b) flow in the shear layer: current streamlines and graph of v_ζ^* at constant values of y^* .

close themselves up; these $O(1)$ currents cannot be extracted either by the outer [$j^{*(E)} = O(1/\text{Ha})$] or inner ($j^{*(C)} = 0$) core regions, nor by the HW layers, which carry an electric current in agreement with the flow *ad infinitum* [5].

The emergence of Hunt's wake leads to a considerable increase of the drag coefficient. The progressive formation of a *ghost* cylinder at rest encapsulating the sphere leads to very strong velocity gradients with the outer core region. These gradients are smoothed over the δ_{SL}^* -thin shear layer, leading to an intensifying tangential stress with increasing Ha . The overall drag coefficient can be then defined as

$$C_d = C_{d,\text{hydro}} + C_{d,\text{em}}, \quad (13)$$

where $C_{d,\text{hydro}}$ corresponds to the purely hydrodynamic drag coefficient, described, e.g., by correlation (12), and $C_{d,\text{em}}$ is the electromagnetic drag coefficient. Note that for the sake of consistency with the pure hydrodynamic case, where C_d is given with respect to the particle Reynolds number, the electromagnetic drag coefficient, so introduced here, is also expressed with respect to particle numbers, in the light of the HL68 model [30]:

$$C_{d,\text{em,Hunt}} = 8 \frac{\text{Ha}_p}{\text{Re}_p} = 8 \left(\frac{N_p}{\text{Re}_p} \right)^{0.5} \quad \text{for } \text{Ha}_p \gg \text{Re}_p, \text{Ha}_p \gg 1. \quad (14)$$

In the literature, other analytical works allow us to complete the HL68 model especially when considering the drag coefficient. For instance, the case $N_p \ll 1, \text{Re}_p \gg 1$ has been solved [31], leading to

$$C_{d,\text{em,Reitz}} = \frac{3}{10} N_p \quad \text{for } N_p \ll 1, \text{Re}_p \gg 1. \quad (15)$$

Let us now turn to the most significant numerical results available, which extrapolate analytical predictions to other values of $(\text{Re}, \text{Ha}, N)$.

In every numerical simulation of MHD flows, one challenging issue is connected to the modeling of the Hartmann layers. The fact that the typical thickness of these layers is $O(1/\text{Ha})$ means that they can become very thin relative to the typical size of the numerical layout. However, as it has been previously enhanced, Hartmann layers exert an active control over the bulk flow. Despite their

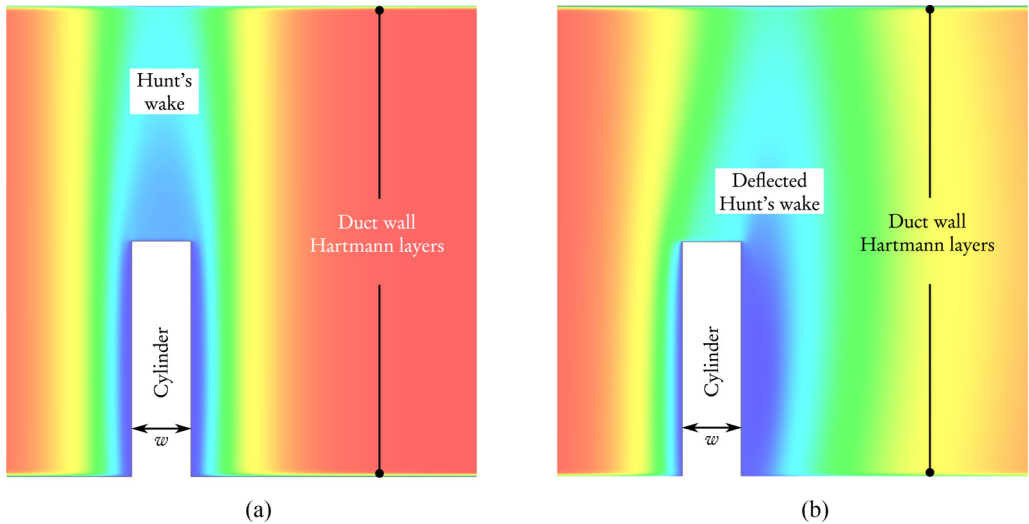


FIG. 5. Hunt's wake past a truncated cylinder [24,29], at $\text{Ha} = 200$, for different $\text{Re}_w = \rho V w / \eta$ (flow from left to right, $d = w$, color scale: higher magnitude from blue to red). (a) Streamwise velocity magnitude, $\text{Re}_w = 1$; (b) streamwise velocity magnitude, $\text{Re}_w = 50$.

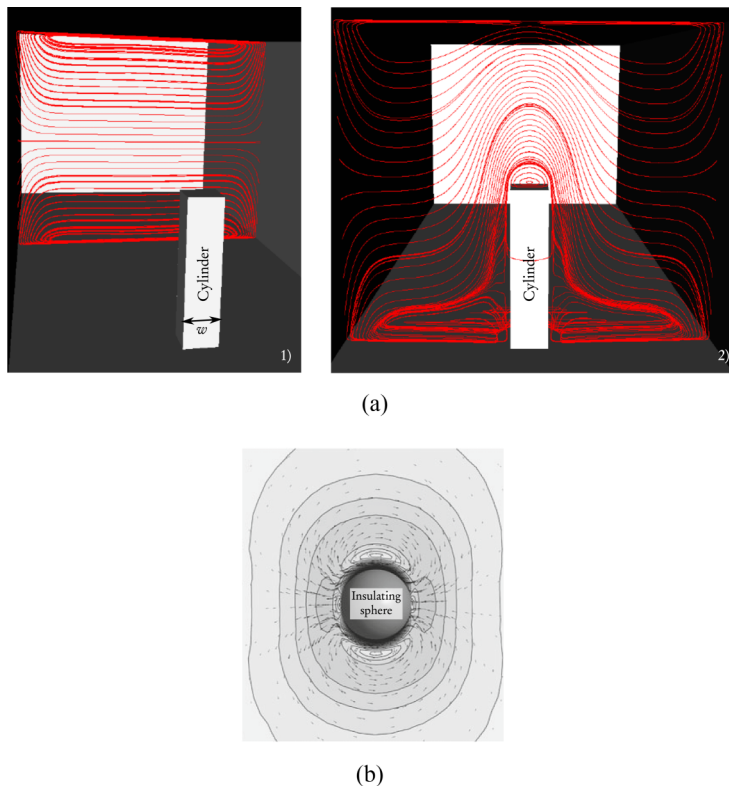


FIG. 6. Original MHD flow patterns past obstacles of various shapes. (a) Electric current density streamlines of the MHD flow past a truncated cylinder [24,29], $Re_w = \rho V w / \eta = 100$, $Ha = 100$. (1) Upstream of the obstacle, (2) across the obstacle. Out-of-plane flow from back to front; (b) current density vectors (arrows) and magnitude (grayscale) in the vicinity of an insulating sphere [23]: $Re_p = 10$, $Ha_p = 2$.

thinness, it is of importance to mesh them properly, so that the essential physics of MHD core flow is captured. An alternative approach is to use wall functions [21,32]. Provided this issue is correctly addressed, the numerical simulations allow us to extrapolate the results obtained in the latter asymptotic theory for different N values.

In a rather different context, Dousset and coworkers [24,29] have numerically confirmed the progressive emergence of Hunt's wake. In this case, the obstacle consists of a truncated square cylinder, and the body Reynolds number Re_w is based on the width w of the cylinder. Depending on the Re_w value, a blocked liquid column arises, standing above the cylinder, from the upper face up to the top Hartmann wall [see Fig. 5(a)]. Outside this region, the flow is found to be quasi-2-D. When Re_w is increased for a given outer magnetic field, Hunt's wake is gradually pushed downstream by the free stream [see Fig. 5(b)]. The flow may thus switch from a vertical (electromagnetic) to a horizontal (hydrodynamic) steady wake. To our knowledge, this is the only numerical evidence of Hunt's wake available in the literature. An experimental counterpart to this study is proposed by Andreev *et al.* [34] for small Ha values (up to 14). In addition to the velocity profiles, the typical distribution of electric current densities and Lorentz force past an obstacle can be determined, as shown in Fig. 6. The results of Dousset *et al.* [24,29] show the electric current streamlines in different cross sections of the duct, located upstream, across, and downstream (not shown) of the obstacle, for moderate Ha values. Upstream of the cylinder [Fig. 6(a)1], the characteristic flow patterns of the Shercliff flow [33] are observed. Similarly, downstream of the cylinder, the perturbations induced by the obstacle gradually dissipates, and the Shercliff flow patterns are gradually recovered (not

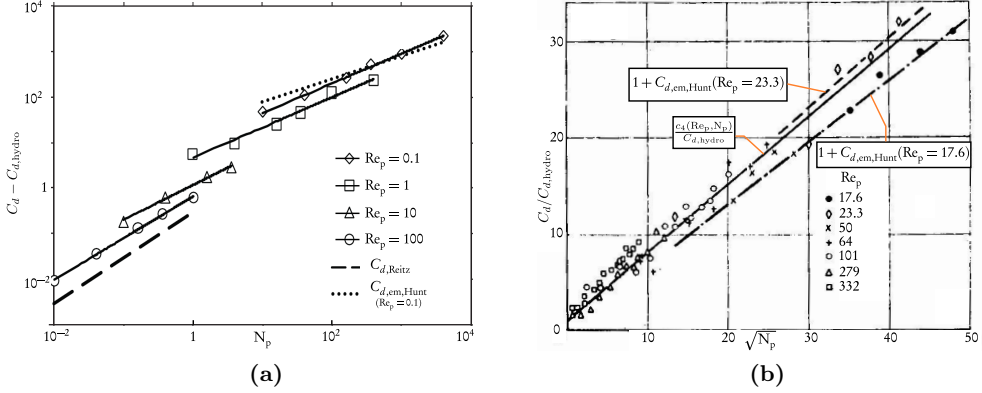


FIG. 7. Drag coefficients of spheres placed in a MHD flow: numerical and experimental results. (a) Drag coefficient: numerical simulations [23]; (b) drag coefficient: experimental data [5,35].

shown). With respect to the section across the cylinder [Fig. 6(a)2], the electric current streamlines accumulate in the region above the cylinder tip, which explains the flow braking observed with the emergence of Hunt's wake. Finally, at the trailing edge of the cylinder upper face, the flow washes down into the rear of the cylinder. Dousset and Poth erat [29] and Andreev *et al.* [34] showed that a small amount of inertia was enough to destroy Hunt's wake, but that the structure of the wake was still strongly determined by electromagnetic effects. The question of high- Ha regimes was left open.

In parallel, two numerical studies have been recently issued by Haverkort and Peeters, about magnetohydrodynamic flows past insulating spheres at low-to-moderate Ha_p values ($Ha_p < 20$) [3,23]. To the best of our knowledge, these papers constitute the only numerical studies focusing on a physical layout fairly close to the sphere MHD problem. There is a major difference, though, which is the implementation of free-slip boundary conditions at the domain boundaries (see Sec. 1A). Their main results show that the distribution of electric currents past the sphere [Fig. 6(b)] is responsible for an increase of the drag coefficient with increasing Ha , due to velocity gradients along the azimuthal direction. The evolution of the drag coefficient with respect to N_p is shown in Fig. 7(a). The drag coefficients calculated from Eqs. (14) and (15) are also indicated as asymptotic references, and the agreement between the numerical modeling and the theoretical predictions seems quite satisfying. As expected, for a given Re_p , the electromagnetic drag coefficient increases with N_p , and this evolution is satisfyingly fitted with a power function of the parameter N_p :

$$C_{d,em} = f(Re_p)N_p^n.$$

Let us now end this review with some significant experimental results. The most challenging issue faced by MHD experiments is the opaque nature of the liquid metals involved, as soon as high Ha values are used. Access to the velocity field is nevertheless possible, but it requires more sophisticated methods, such as ultrasound Doppler velocimetry [18] (UDV), electric potential velocimetry [36] (EPV), or x-ray radioscopy [37]. In the case of the drag on spheres immersed in a liquid metal, in the presence of a strong transverse magnetic field, a reference study carried out by Branover *et al.* [35] has given rise to the following empirical law for the global drag coefficient, valid for a wide range of (Re_p , Ha_p , N_p) values in most practical cases:

$$C_{d,Br} = c_4(Re_p, N_p) = C_{d,hydro}(Re_p)(1 + 0.7\sqrt{N_p}), \quad \forall (Re_p, Ha_p, N_p). \quad (16)$$

The experimental results found by Branover *et al.* [35], along with the correlation (16), are displayed in Fig. 7(b). For the sake of comparison, the two curves corresponding to the drag coefficient

calculated from Eq. (14) at $Re_p = 17.6$ and $Re_p = 23.3$ are also shown. The agreement is found excellent between experimental results and theoretical predictions.

The previous review has allowed us to sum up the state of the art of the most salient physical features related to (magneto)hydrodynamic flows around past obstacles. Let us now turn to the physical modeling of the suspending sphere MHD problem.

II. PHYSICAL MODELING

A. Notations and assumptions

The MHD flow under consideration is supposed to be a permanent, incompressible viscous Newtonian flow given a homogeneous and constant temperature T , so that its physical properties ρ , η , and σ are assumed to be constant. A typical working fluid is galinstan (Table I), so that the classical quasistatic and low-Rm approximations are verified, allowing us to disregard displacement currents and to write the electromotive current and Lorentz force terms with respect to the outer magnetic field \vec{B}_0 only [38].

The steady quantities of interest are expressed in the Cartesian system of coordinates: First, the velocity field $\vec{v} = v_x(\vec{x})\vec{e}_x + v_y(\vec{x})\vec{e}_y + v_z(\vec{x})\vec{e}_z$, then, the pressure $p = p(x, y, z)$, and at length, the electric current densities $\vec{j} = j_x(\vec{x})\vec{e}_x + j_y(\vec{x})\vec{e}_y + j_z(\vec{x})\vec{e}_z$, the latter being deduced from the electric potential $\phi = \phi(x, y, z)$.

All the bulk physical quantities are scaled with a typical duct length L , which turns out to be more convenient to discuss bulk flow patterns (e.g., influence of the Hartmann layers on the core-flow), while d is more convenient for describing phenomena acting in the vicinity of the sphere (e.g., drag coefficient). The latter observation explains why a mixed terminology between bulk and particle dimensionless numbers is adopted in the present article.

The dimensionless quantities of interest, superscripted $*$, are defined as follows:

- (1) the Cartesian system of coordinates: $-5d/L \leq x^* = x/L \leq 15d/L$, $-1 \leq y^* = y/L \leq 1$ and $-1 \leq z^* = z/L \leq 1$;
- (2) velocity $\vec{v}^* = \vec{v}/V$, where V corresponds to the maximum value of the inlet velocity;
- (3) pressure $p^* = p/\rho V^2$;
- (4) vorticity $\vec{\omega}^* = \vec{\omega}L/V$;
- (5) electric potential $\phi^* = \phi/LB_0V$; and finally
- (6) electric current densities: $\vec{j}^* = \vec{j}/\sigma VB_0$.

B. Geometry

The typical geometrical layout is given in Fig. 8, along with the electromagnetic and hydrodynamic boundary conditions (BCs). The sphere with diameter $d = 10^{-2}\text{m}$ is placed in the duct,

TABLE I. Physical properties of galinstan [39,40].

Property	Galinstan
Boiling point ($^{\circ}\text{C}$)	> 1300
Melting point ($^{\circ}\text{C}$)	-19
Vapor pressure (Pa)	$< 10^{-6}$ (at 500°C)
Water compatibility	Insoluble
Density (kg m^{-3})	6360 (room temperature)
Dynamic viscosity (Pa s)	2.14×10^{-3} (RT)
Electrical conductivity (S m^{-1})	3.29×10^6 (RT)
Magnetic permeability (H m^{-1})	$4\pi \times 10^{-7}$
Surface tension (N m^{-1})	5.35×10^{-1} (RT)

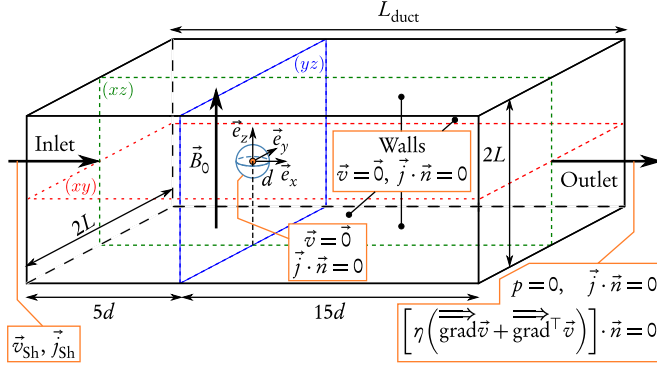


FIG. 8. Geometry (not to scale), boundary conditions, and cutting planes for post-treatment.

whose typical length $L = 4d$ is the half-height of the square cross section. The flow, far enough from the sphere, is directed along the \vec{e}_x direction, while the outer magnetic field is oriented along the \vec{e}_z direction. The blockage ratio is $\lambda = d/2L = 1/8$. The origin of the Cartesian system of coordinates $(O, \vec{e}_x, \vec{e}_y, \vec{e}_z)$ is located at the center of the spherical inclusion. The latter is axially offset upstream by a distance $5d$ relative to the center of the duct, whose length is $L_{\text{duct}} = 20d$. As such, the inlet is located a distance $5d$ upstream the sphere, and the outlet is located a distance $15d$ downstream, so that the development of the wake at the rear of the sphere is undisturbed by the outlet boundary condition [41] (see also a sensitivity analysis to the distance downstream in Appendix C). The following cutting planes are defined for data postprocessing, as shown in Fig. 8: (xz) , (xy) , and (yz) are planes passing through the origin, respectively. Other cutting planes may be defined in the analysis: The planes parallel to (xz) and located at a given coordinate $y^* = y_0$ are denoted $(xz)_{y_0}$, and the same notation holds for $(xy)_{z_0}$ (with $z^* = z_0$) and $(yz)_{x_0}$ (with $x^* = x_0$).

C. Mathematical model

A potential formulation based on the electric potential ϕ is chosen. All the electromagnetic quantities can actually be derived from ϕ . The basic dimensionless MHD equations are written [5,38]

$$\Delta^* \phi^* = \text{div}^*(\vec{v}^* \times \vec{e}_z), \quad (17)$$

$$(\vec{v}^* \cdot \overrightarrow{\text{grad}}^*) \vec{v}^* = -\overrightarrow{\text{grad}}^* p^* + \frac{1}{\text{Re}} \overrightarrow{\Delta}^* \vec{v}^* + \frac{\text{Ha}^2}{\text{Re}} \vec{j}^* \times \vec{e}_z. \quad (18)$$

These equations are completed by the Ohm's law for the electric current densities,

$$\vec{j}^* = -\overrightarrow{\text{grad}}^*(\phi^*) + \vec{v}^* \times \vec{e}_z, \quad (19)$$

and by the conservation equations,

$$\text{div}^*(\vec{v}^*) = 0, \quad \text{div}^*(\vec{j}^*) = 0. \quad (20)$$

The duct walls and the sphere are considered electrically insulated, so that the following condition is applied at the boundaries (\vec{n} being the outward normal unit vector):

$$\vec{j}^* \cdot \vec{n} = 0. \quad (21)$$

The electromagnetic boundary condition at the inlet of the duct section must be consistent with the fully established Shercliff flow [33]:

$$\vec{j}^*|_{\text{inlet}} = \vec{j}_{\text{Sh}}^*. \quad (22)$$

In practice, preliminary 3-D computations of the duct flow without the immersed body are performed at a prescribed initial Re_p value, until the fully established state is reached. The resulting current density profiles in the duct cross section are then extracted, benchmarked with the Shercliff profiles, and applied safely as the inlet boundary condition for the current density. Finally, at the outlet, it is usual to implement the following BC for \vec{j} :

$$\vec{j}^* \cdot \vec{n}|_{\text{outlet}} = 0. \quad (23)$$

As specified in the literature dedicated to MHD flows around obstacles (see, e.g., Refs. [21,24]), this BC is formally exact only when averaged across the outlet. However, we apply it locally, which results in neglecting the currents normal to the outlet. These currents are of order $1/Ha$, so this approximation remains relevant as long as $Ha \gg 1$, whatever the distance between the obstacle and the outlet cross section is. For small Ha values, a “buffer” region can be introduced, where the perturbations induced by the presence of the obstacle may freely expand, until they are totally damped. In the latter case, the Shercliff flow is physically representative of the flow patterns at the outlet, and Eq. (23) can be implemented as the outlet electromagnetic BC. In the present paper, a $15d$ -long buffer region at the rear of the sphere has been found long enough to apply locally this condition with no loss of generality.

As far as BCs are concerned, a no-slip condition is applied at the duct walls and along the surface of the sphere:

$$\vec{v}^* = \vec{0}. \quad (24)$$

As previously enhanced for current densities, the inlet velocity must be consistent with the fully established Shercliff flow. The inlet velocity profiles are recovered from the preliminary computations previously mentioned. When the fully established regime is obtained, the final V and Re_p values are known, and the benchmarked velocity profiles are applied as the inlet BC for the velocity:

$$\vec{v}^*|_{\text{inlet}} = \vec{v}_{\text{Sh}}^*. \quad (25)$$

The outlet boundary condition is chosen so that the convection of flow structures through the outlet of the pipe section is eased, without causing artificial flow distortions. To this end, a zero-pressure, no-viscous-stress boundary condition is implemented at the outlet:

$$p_{\text{outlet}}^* = 0, \left(\overrightarrow{\text{grad}}^* \vec{v}^* + \overrightarrow{\text{grad}}^{*\top} \vec{v}^* \right) \cdot \vec{n}|_{\text{outlet}} = 0. \quad (26)$$

D. Numerical implementation

The numerical approach developed here is mostly inspired from the one described in another paper [42]. As the finite-element method (FEM) is chosen, the discretization of previous equations bears on the determination of associated weak forms. The discretization of Eqs. (17) (in fact, a Poisson equation for the electric potential) and (20) (continuity) are classical study cases in FEM-based formulations. The discretization of Eq. (18) (Navier-Stokes equations) is performed through a pressure-correction scheme deriving from the semi-implicit method for pressure linked equations (SIMPLE) [43], suitable for laminar flows.

The nonlinear physical problem is linearized by using the Newton-Raphson method. A segregated solver is used, which treats the equations sequentially. One advantage is that a lower CPU cost is required, the main drawback being the induction of an artificial numerical damping between the flow equations, which is addressed by means of optimization algorithms deriving from Levenberg-Marquardt algorithm [44]. There are two segregated steps to solve the linearized problem, the first of which involves the hydrodynamic variables, \vec{v}^* and p^* . It is based on an iterative linear system solver referred to as general minimum residual (GMRES) solver [45]. The second segregated step involves the electric potential ϕ^* alone, and given the quite basic weak form of the Poisson induction equation, a direct linear system solver is used. The latter is based on the the

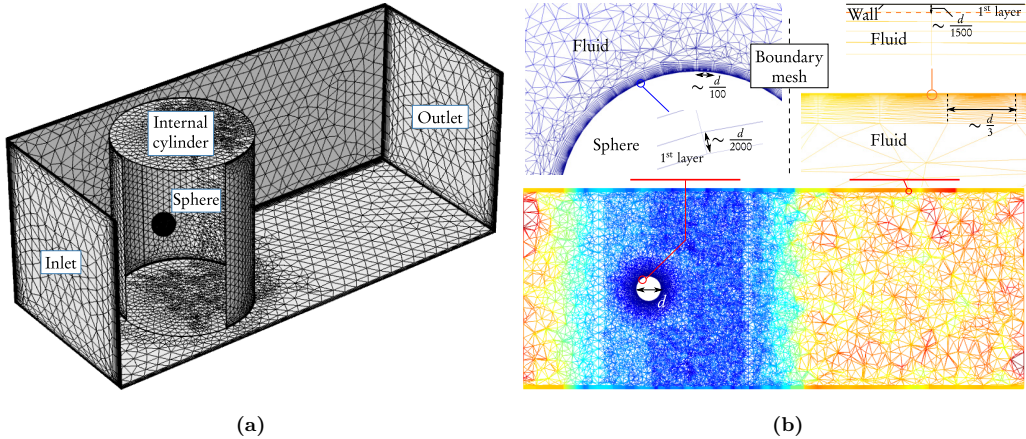


FIG. 9. Mesh used for the 3-D numerical computation ($\sim 9 \times 10^5$ elements). (a) Global view; (b) mesh size and close-up view of the boundary layers in (xz) . Color scale: mesh density from blue (extrafine) to red (coarse). d stands for the sphere diameter.

multifrontal massively parallel sparse direct solver (MUMPS), using lower-upper (LU) factorization [46].

An overall view of the implemented mesh is displayed in Fig. 9(a). It consists of approximately 9×10^5 elements, mainly tetrahedral, with specific mesh refinement at strategic locations. Thus, a provided hexahedral or prismatic boundary layer mesh is set up at the boundaries of the fluid domain, i.e., near the duct walls, and near the surface of the sphere. Typically, the relative thickness of the first layer is set so as to be much lower than the reciprocal of the maximum Hartmann and Reynolds numbers, which both monitor the thickness of the physical boundary layers in asymptotic conditions ($Ha \gg 1$, $Ha \rightarrow 0$). Finally, the state of the art in the previous section leads us to expect different flow regimes, switching from a hydrodynamic horizontal wake to an electromagnetic vertical wake, creating a “ghost” [24,29] cylinder on both sides of the obstacle. The emergence of such atypical flow patterns has been taken into account in our meshing strategy: an “internal cylinder” area is designed, extending from the bottom wall to the top wall, where the mesh density is set finer [see Fig. 9(b)]. This cylinder is off-centred relative to the sphere, to allow for the lengthening of the steady hydrodynamic wake at the rear of the sphere. Let us finally point out that the numerical precision of the code has been assessed by performing mesh convergence tests.

III. RESULTS AND INTERPRETATION

In this section, the evolution of the most salient flow patterns and of the flow coefficient values with respect to (Re_p, Ha) are highlighted. The following numerical developments are initially benchmarked in the purely hydrodynamical case which corresponds to the asymptotic case, $Ha = 0$ (see Appendix B).

A. Flow patterns for $N_p \lesssim 1$

The addition of an outer magnetic field such as $N_p \lesssim 1$ clearly alters the hydrodynamic flow patterns. As shown in Figs. 10(a) and 10(b), for a given Re_p value, increasing Ha (and thus N_p) contributes to the emergence of a ghost obstacle. The latter consists of a blocked area circumscribing the sphere and tending to span along the height of the duct for a larger N_p [see Fig. 13(a) for $N_p \gg 1$]. In contrast, for a given N_p value, increasing Re_p leads to the gradual advection of this obstacle by the main stream, and for $N_p \ll 1$ the hydrodynamic flow patterns discussed in Fig. 18 are recovered. Besides, for some values of the triplet (Re_p, Ha, N_p) , typically when N_p is small and

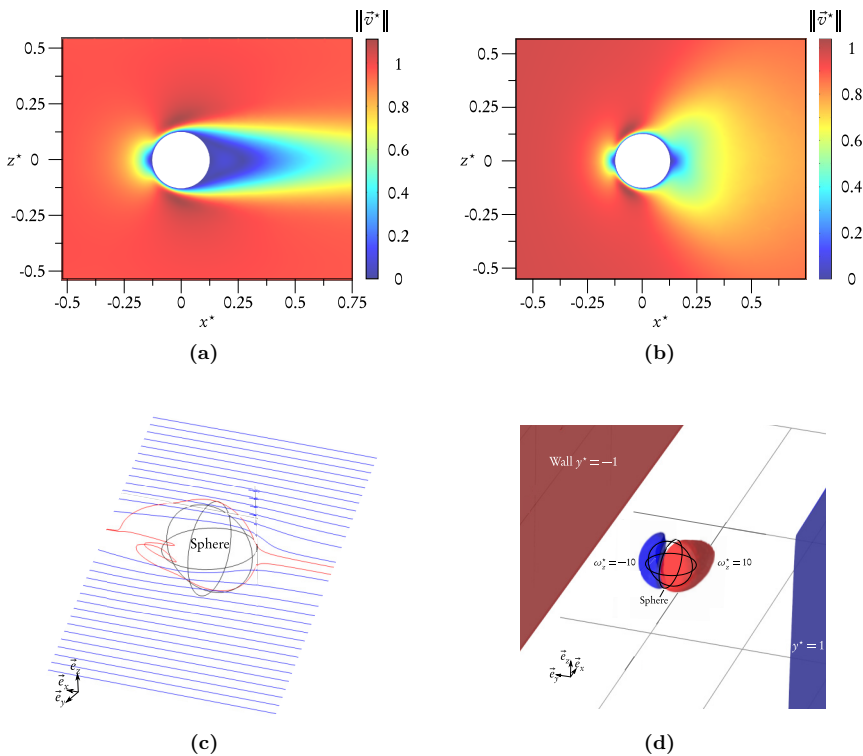


FIG. 10. Magneto hydrodynamic flow patterns around the sphere for $N_p \lesssim 1$. (a) Norm (color scale) of the velocity field \vec{v}^* in (xz) , for $(\text{Re}_p, \text{Ha}, N_p) = (113.2, 15, 0.12)$; (b) norm (color scale) of the velocity field \vec{v}^* in (xz) , for $(\text{Re}_p, \text{Ha}, N_p) = (113.2, 90, 4.47)$; (c) \vec{v}^* streamlines, for $(\text{Re}_p, \text{Ha}, N_p) = (113.2, 15, 0.12)$: recirculation region in (xz) (red) and (xy) (blue); (d) $\omega_z^* = 10$ (resp. -10) isosurfaces in red (resp. blue), for $(\text{Re}_p, \text{Ha}, N_p) = (113.2, 15, 0.12)$.

Re_p is large, flow separation and electromagnetically altered recirculating areas can be noticed at the rear of the sphere, as shown in Fig. 10(c). However, for moderate values of N_p ($N_p \lesssim 1$), the shape of the lateral free shear layers (given by isosurfaces of z vorticity, ω_z^*) is not significantly different from the purely hydrodynamic case (“wing” pattern), as displayed in Fig. 10(d).

The emergence of the ghost obstacle makes the flow switch from horizontal to vertical sphere wake configuration. The transition regime can also be emphasized by focusing on the velocity contours at the rear of the sphere, in different planes, as in Fig. 11. There is a noticeable asymmetry between cutting planes (xy) [Fig. 11(a)] and (xz) [Fig. 11(b)]. The spreading of velocity contours along the outer field direction \vec{e}_z is observed, a phenomenon also highlighted by Haverkort *et al.* [23], for similar (Ha, Re_p) values.

With respect to electromagnetic quantities, the current densities in different cutting planes are shown in Fig. 12. First, in the plane (xy) perpendicular to \vec{B}_0 [Fig. 12(a)], the electric currents are found to be oriented mainly along the \vec{e}_y direction, and at quite a large distance from the sphere. This electric current generates a z -Lorentz force $f_{L,x}^*$ which tends to accelerate the fluid on both sides of the sphere. Now, in the plane (yz) parallel to the outer magnetic field, it is shown in Fig. 12(b) that the electric currents are positive along \vec{e}_y only in the top and bottom Hartmann layers, while they become negative a little further away. Thus, an electromagnetic braking due to the Lorentz force is induced in areas that are far from the sphere, favoring the wake expansion previously highlighted. These observations are in agreement with Haverkort *et al.* [23] [Fig. 6(b)]. They testify from the gradual emergence of the ghost obstacle, which is enhanced in the following section by investigating high- N_p regimes.

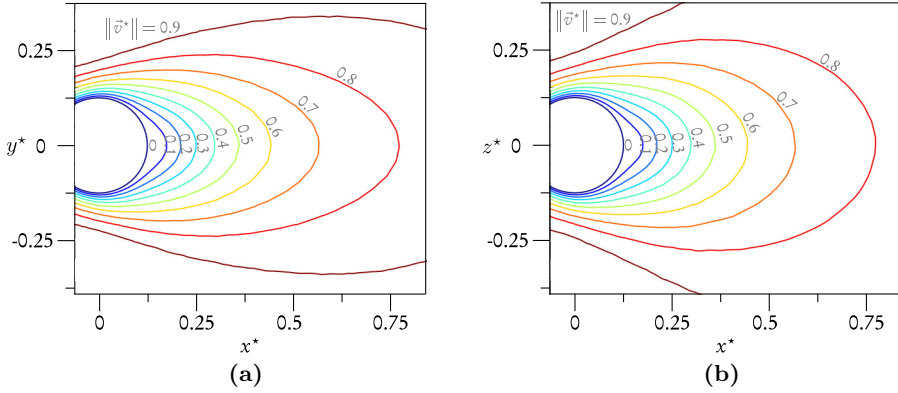


FIG. 11. Slight asymmetry of the sphere wake for $N_p \lesssim 1$, preferentially oriented along the field lines. (a) \vec{v}^* contours: sphere wake in (xy) , $(\text{Re}_p, \text{Ha}, N_p) = (8, 7, 0.38)$; (b) \vec{v}^* contours: sphere wake in (xz) , $(\text{Re}_p, \text{Ha}, N_p) = (8, 7, 0.38)$.

B. Flow patterns for $N_p \gg 1$

Let us further increase the value of the outer magnetic field, so that the particle Stuart number N_p fulfills the condition $N_p \gg 1$. The MHD flow patterns linked to this flow regime are displayed in Fig. 13. In this asymptotic regime, the validity of numerical simulations is benchmarked with Hunt and Ludford's study (see Sec. IC 3). As shown in Fig. 13(a), Hunt's (vertical) wake is actually observed for $(\text{Re}_p, \text{Ha}, N_p) = (2.2, 200, 1136.4)$, leading to the formation of a "ghost" cylinder circumscribing the sphere. The emergence of this cylinder spanning over the height of the duct, now well established compared to the intermediate flow regime of Fig. 10, constitutes a much more consequent flow obstacle than the original sphere. Apart from the work of Dousset and coworkers [24,29] in the case of truncated cylinders (see Fig. 5), there seems to be no numerical evidence of this wake in the literature. As seen in Fig. 13(b), mass conservation implies that the flow is accelerated between the ghost cylinder and the side walls of the channel; besides, typical Shercliff flow patterns are recovered downstream, far from the sphere.

In this $N_p \gg 1$ flow regime, no separated flow can be observed: The recirculating areas are indeed electromagnetically damped, and the well-known MHD tendency toward two-dimensionality tends

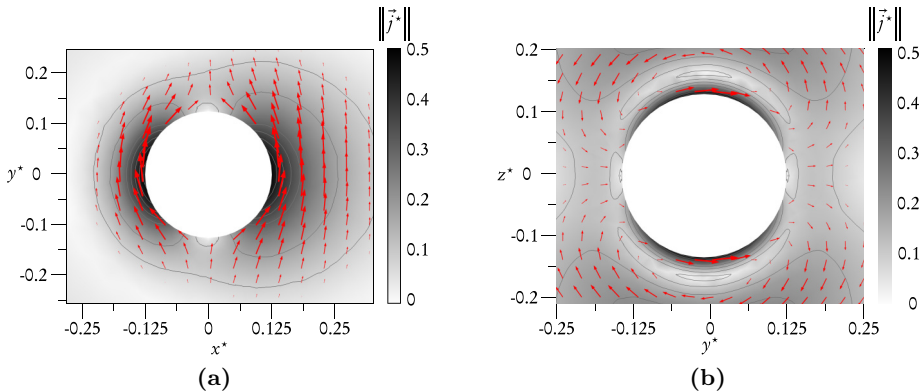


FIG. 12. Current density patterns for $N_p \lesssim 1$. (a) \vec{j}^* norm (grayscale), contours and scaled arrows in (xy) for $(\text{Re}_p, \text{Ha}, N_p) = (8, 7, 0.38)$; (b) \vec{j}^* norm (grayscale), contours and scaled arrows in (xz) in (yz) for $(\text{Re}_p, \text{Ha}, N_p) = (8, 7, 0.38)$.

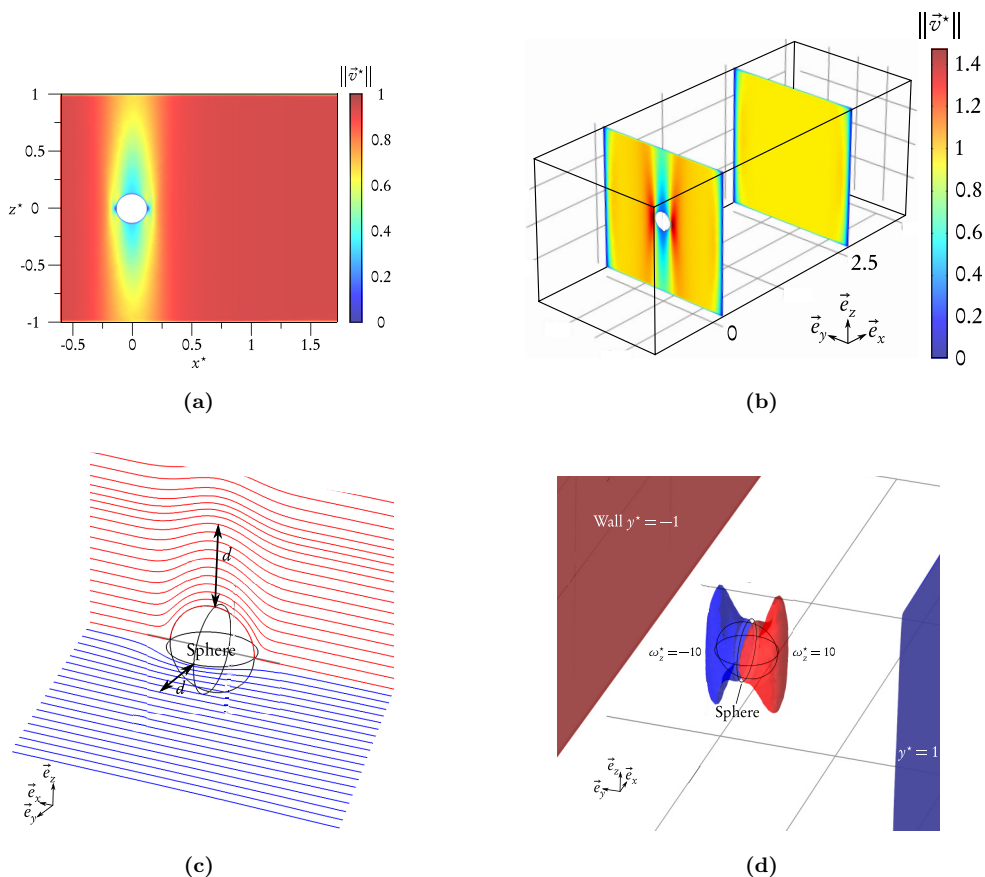


FIG. 13. Magnetohydrodynamic flow patterns around the sphere for $N_p \gg 1$. (a) Hunt's wake (color scale) seen in (xz) , for $(Re_p, Ha, N_p) = (2.2, 200, 1136.4)$; (b) Hunt's wake in (yz) and Shercliff flow in $(yz)_{2.5}$ (slice view), $(Re_p, Ha, N_p) = (2.2, 200, 1136.4)$; (c) \vec{v}^* streamlines: (xz) (red) and (xy) (blue), for $(Re_p, Ha, N_p) = (2.2, 200, 1136.4)$; (d) $\omega_z^* = 10$ (resp. -10) isosurfaces in red (resp. blue), for $(Re_p, Ha, N_p) = (2.2, 200, 1136.4)$.

to favor the stretching of vortices aligned with the direction of the outer magnetic field, i.e., the \vec{e}_z axis. Consequently, the other components of vorticity being damped, the recirculating flow at the rear of the sphere vanishes at high N_p values, as shown in Fig. 13(c), where the presence of the ghost obstacle distorts the velocity streamlines in (xz) significantly further away from the sphere than in (xy) . Moreover, this 2-D tendency changes the shape of the lateral free shear layers. As shown in Fig. 13(d), the iso- ω_z^* pattern is stretching according to a saddle shape, in contrast with the wing shape of Fig. 10(d). This leads to the emergence of Shercliff (parallel) layers [22] (see Figs. 3 and 4), which contribute to the gradual generation of the ghost cylinder and prevents the fluid from penetrating the blocked column.

Now, concerning current density patterns, the emergence of the shear parallel layer is made evident in Fig. 14(a). As expected, the electric currents flow through the Hartmann layers near the top and the bottom duct walls, in the positive \vec{e}_y direction. In the vicinity of the sphere, two distinct layers can be noticed. The Hartmann layers, near the top and the bottom of the sphere, carry an azimuthal electric current. The development of the shear layer is noticeable in the inset, circumscribing the sphere and the ghost cylinder. In this layer, the currents are mainly oriented

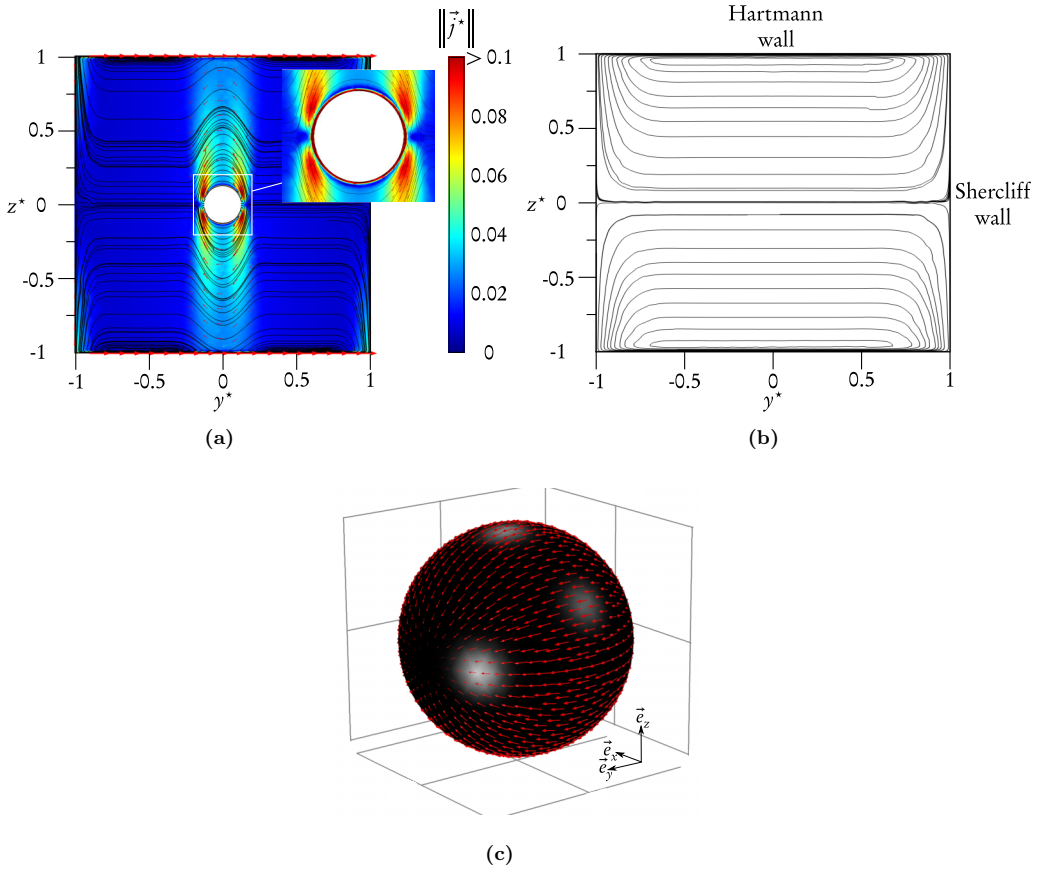


FIG. 14. Current density flow patterns for $N \gg 1$. (a) Electric current density patterns (magnitude, streamlines, and arrows): emergence of the shear parallel layer, in (yz) , for $(\text{Re}_p, \text{Ha}, N_p) = (2.2, 200, 1136.4)$. Inset: close-up view of the Hartmann layer near the sphere surface; (b) electric current streamlines in $(yz)_1$: Shercliff flow patterns, $(\text{Re}_p, \text{Ha}, N_p) = (11.2, 100, 55.8)$; (c) electric current densities along the surface of the sphere ($y^* > 0$ view), $(\text{Re}_p, \text{Ha}, N_p) = (11.2, 100, 55.8)$.

(positive and negative) along the outer magnetic field direction. In agreement with the HL68 model, the electric current streamlines are clearly rejected from the inner core region [similar to Dousset's results; see Fig. 6(a)]. Along with the previous remarks concerning velocity patterns, the present analysis of current density patterns constitutes, to our knowledge, the first numerical evidence of the shear layer development.

Note that in the equatorial (xy) plane of the sphere, the arising of a boundary-layer singularity could be suspected, owing to the fact that the wall becomes locally aligned with the magnetic field. As indicated in the inset of Fig. 14(a), such a singularity, made evident for the first time by Roberts [47] in the case of an insulating circular duct, here remains to be demonstrated. A decisive proof of its existence would essentially rely on the possibility to consider sufficiently large particle Hartmann numbers (singularity thickness $\sim \text{Ha}_p^{-2/3}$).

Finally, electric current streamlines typical of Shercliff flow topology are recovered downstream, far from the obstacle, as seen in Fig. 14(b), which is another benchmark for the present results. At the surface of the sphere, the current densities are oriented along the positive \vec{e}_y direction [see Fig. 14(c)], in accordance with the currents carried by the Hartmann layers.

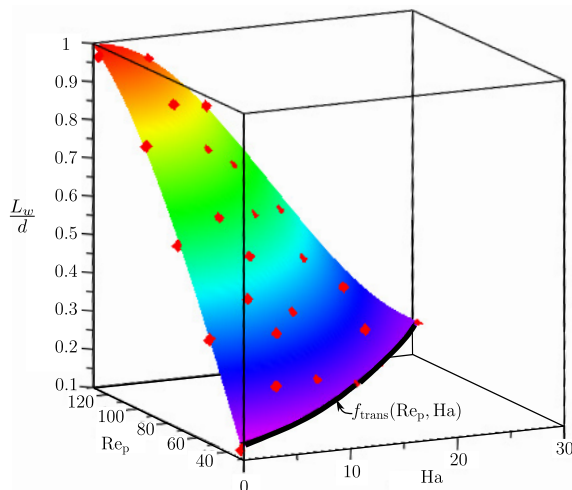


FIG. 15. (Horizontal) wake length with respect to various (Ha, Re_p) values. Color scale: parametrized surface; red symbols: numerical simulations. $f_{\text{trans.}}(Re_p, Ha)$ represents the transition curve between simulations showing no recirculating areas and those immediately following and showing such recirculating flow patterns.

C. Flow coefficients

Wake length. The addition of an outer electromagnetic field tends to turn the horizontal sphere wake into a vertical Hunt's wake. The sphere wake length thus decreases with increasing Ha values, at given Re_p . Let us try to establish a correlation for $L_w(Re_p, Ha)$, which is an original result regarding the literature.

The results are displayed in Fig. 15. In this figure, the symbols (\diamond) stand for the set of numerical simulations where flow separation occurs and recirculating areas exist, while the colored area represents the parametrized surface $L_w/d = c_{L_w}(Re_p, Ha)$ fitted on the data points. The solid line $f_{\text{trans.}}(Re_p, Ha)$ represents the transition curve between simulations showing no recirculating areas and those immediately following and showing such recirculating flow patterns. A bicubic interpolation gives the following expression for the correlation c_{L_w} , with a mean error smaller than 2%, for $Re_p \in [30..130]$, $Ha \in [0..30]$:

$$c_{L_w}(Re_p, Ha) = \sum_{\substack{i, j=0..3 \\ i+j \leq 3}} \alpha^{(i,j)} Re_p^i Ha^j, \quad (27)$$

where the $\alpha^{(i,j)}$ coefficients are given in Table II. Obviously, this correlation should be benchmarked by other numerical results for the same typical geometry.

Drag coefficient. The emergence of a ghost obstacle leads to the increase of C_d with Ha or N_p , at given Re_p , the contribution of the electromagnetic part of the drag coefficient, $C_{d,\text{em}}$, becoming gradually preponderant. In this section, we shall try to establish one correlation for $C_d(Re_p, N_p)$ rather than $C_d(Re_p, Ha)$, because the existing literature consistently focuses on (Re_p, N_p) pairs concerning the MHD drag coefficient (see Sec. IC).

First, let us draw the evolution of the drag coefficient with respect to N_p for given Re_p values, as shown in Fig. 16. On the one hand, a reasonable agreement with the results of Haverkort *et al.* [23] can be found, when compared with Fig. 7(a). On the other hand, three distinct areas can be clearly distinguished, depending on the value of N_p . For $N_p \ll 1$, the electromagnetic drag coefficient approaches the potential theory limit linked with correlation (15), with a typical scaling $C_{d,\text{em}} \sim N_p$. For $N_p \gg 1$, the scaling $C_{d,\text{em}} \sim \sqrt{N_p}$ derived from Hunt and Ludford's theory [see

TABLE II. Coefficients for correlations (27) and (28).

Wake length		Drag coefficient	
(i, j) pair	$\alpha^{(i,j)}$	(i)	$\beta^{(i)}$
(0,0)	$-\frac{32}{125}$	(1)	$\frac{169189}{45612}$
(0,1)	$\frac{577}{50000}$	(2)	$\frac{21704}{52751}$
(1,0)	$\frac{1211}{100000}$	(3)	1
(0,2)	$-\frac{1333}{100000}$	(4)	-1
(2,0)	$\frac{95}{14726399}$	(5)	$-\frac{496888}{6537}$
(0,3)	$\frac{496}{10808455}$	(6)	$\frac{21548}{80261}$
(3,0)	$-\frac{24}{122324159}$	(7)	$-\frac{7164}{384065}$
(1,1)	$-\frac{723}{2072227}$	(8)	$\frac{12219}{21319}$
(1,2)	$-\frac{89}{11825671}$	(9)	$\frac{3643}{10089}$
(2,1)	$\frac{38}{18313253}$	(10)	-1

correlation (14)] is recovered. The scaling change between these two asymptotic regimes occurs at moderate N_p values. Typically, $C_{d,em} \sim N_p^{0.65}$ in this transitional area testifying from the gradual switch from horizontal hydrodynamic wake to vertical Hunt's wake. This also partially confirms the $C_{d,em} = f(\text{Re}_p)N_p^n$ correlation proposed by Haverkort.

Now, let us determine one correlation $C_{d,em} = c_{C_{d,em}}(\text{Re}_p, N_p)$ for the electromagnetic drag coefficient. We first tried to interpolate a function of the kind $f(\text{Re}_p)N_p^n$, as suggested by Haverkort, and then the correlation of Branover *et al.* [see Eq. (16)]. In both cases, the discrepancy with our results was too high (especially for small N_p values). We then tried to interpolate a function of the kind $f(\text{Re}_p, N_p)N_p^{n(N_p)}$, and we obtained better results. We propose the following expression for the correlation $c_{C_{d,em}}$, whose mean error with respect to our numerical results is 7.9%, for

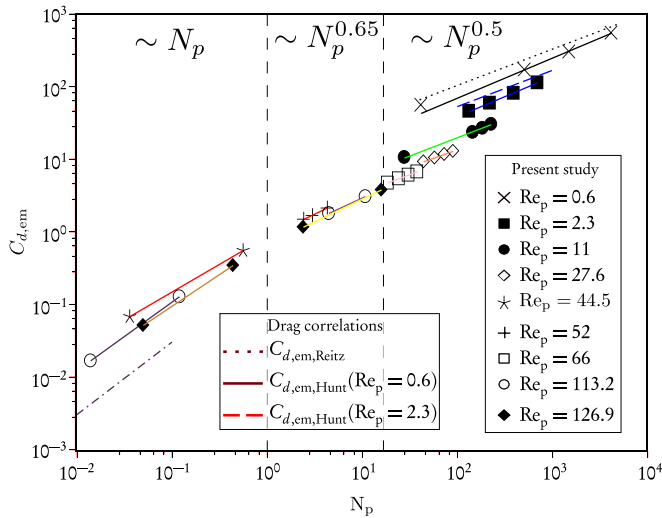


FIG. 16. Electromagnetic drag coefficient with respect to (Re_p, N_p) (see Fig. 7(a) for a comparison with the results of Haverkort *et al.* [23]).

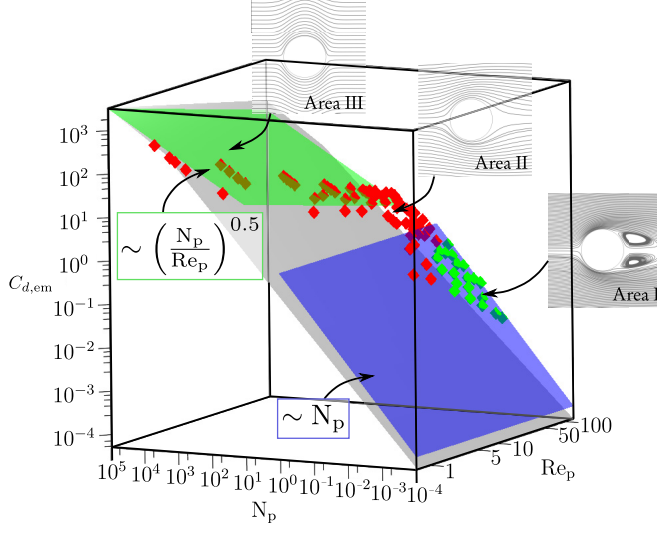


FIG. 17. Electromagnetic drag coefficient with respect to (Re_p, N_p) , and the three resulting flow regimes: I, mainly hydrodynamic flow patterns, horizontal wake, recirculating areas; II, mainly hydrodynamic flow patterns, horizontal wake, no recirculating areas; III, mainly MHD flow patterns, Hunt's (vertical) wake, no recirculating areas. Color scale: gray, surface parametrized according to correlation (28); blue: asymptotic theoretical limit for $N_p \ll 1$ [see (15)]; green: asymptotic theoretical limit for $N_p \gg 1$ [see (14)]. Green symbols: numerical simulations in area I; red symbols: other simulations.

$\text{Re}_p \in [0.6 \dots 130]$ and $N_p \in [10^{-2} \dots 4 \times 10^3]$:

$$c_{C_{d,em}}(\text{Re}_p, N_p) = \left\{ \frac{\beta^{(1)}}{\text{Re}_p^{\beta^{(2)}}} [\beta^{(3)} + \beta^{(4)} \exp(\beta^{(5)} N_p)] + \beta^{(6)} \exp(\beta^{(7)} N_p) \right\} N_p^{\beta^{(8)} + \beta^{(9)} \exp(\beta^{(10)} N_p)}, \quad (28)$$

where the $\beta^{(i)}$ coefficients are given in Table II. Let us extract the asymptotic limits of correlation (28) for $N_p \ll 1$ and $N_p \gg 1$, which yields

$$\lim_{N_p \rightarrow 0} c_{C_{d,em}} = 0.27 N_p^{0.93}, \quad \lim_{N_p \rightarrow +\infty} c_{C_{d,em}} = 3.71 \frac{N_p^{0.57}}{\text{Re}_p^{0.41}}. \quad (29)$$

These limits are in satisfying agreement with the theoretical asymptotic cases (14) ($N_p \gg 1$) and (15) ($N_p \ll 1$), for which $C_{d,em} = 8N_p^{0.5}/\text{Re}_p^{0.5}$ and $C_{d,em} = 0.3N_p$, respectively.

The results are displayed in Fig. 17. In this figure, the gray surface represents correlation (28), and the (red and green) symbols stand for the set of numerical simulations used for fitting. Here, the range of N_p values is intentionally extended to $N_p \in [10^{-2} \dots 4 \times 10^3]$, so that a comparison can be made with the asymptotic theoretical limits for $N_p \ll 1$ [see (15)], represented by the blue plane, and for $N_p \gg 1$ [see (14)], represented by the green plane. A most insightful feature is related to the different flow regimes with respect to (Re_p, N_p) values. A scaling law is established, which permits to distinguish three flow areas.

Area I (green symbols) mainly involves hydrodynamic flow patterns, with horizontal wake due to the presence of a counterclockwise vortex pair for instance. In this area, where $N_p < 1$, the amount of inertia remains high enough to prevent the development of a Hunt's wake, and the isovorticity pattern around the sphere is wing shaped as previously shown. However, the structure of the wake is strongly influenced by the presence of the magnetic field, as small as it can be. Indeed, the value of the electromagnetic drag coefficient becomes gradually comparable with the purely hydrodynamic

one as N_p increases (see Appendix B for further details about purely hydrodynamic benchmarking results). Besides, as it has been noticed in Fig. 15, the wake length is diminishing as H_a (and thus N_p) increases, the vortex pair in the recirculating region is gradually vanishing. If we extrapolate correlation (28) to lower N_p regions, the matching with the potential theory limit (blue plane) seems quite satisfying. As previously highlighted, in this area, a scaling law relates $C_{d,em}$ with N_p^l , l approaching unity in the limit $N_p \ll 1$.

Area II (red symbols around $N_p = 1$, between the upper edge of the blue plane and the lower edge of the green plane) still mainly involves hydrodynamic flow patterns, with horizontal wake, but no more recirculating areas. In this area, where $N_p \sim 1$, electromagnetic effects compete with inertial effects. Typically, the magnetic extinction of the twin vortices at the rear of the sphere is well explained by the presence of two induced electric current loops in the (yz) plane. The decisive role of the Stuart number N_p is consistently made evident by considering that the Joule timescale, $\tau_{\text{Joule}} = \rho/\sigma B_0^2$, becomes smaller than the vortex turnover timescale, $\tau_{\text{turn}} = d/V$, when the magnetic field becomes large enough. As previously highlighted, the profile of the wake becomes asymmetric, with a preferential orientation along the outer field direction. In this case, flow separation is not observed anymore; the structure of the wake shows thus a distinct difference with the one noticed in area I. In this transitional area, a change in the $C_{d,em}$ slope is observed, a scaling law relating $C_{d,em}$ and $f(1/\text{Re}_p^m)N_p^n$ is found, with m approaching 0.4 [according (28)] and n approaching 0.65 (as shown in Fig. 16).

Finally, area III mainly involves MHD flow patterns, with the gradual emergence of the Hunt's (vertical) wake, and no recirculating areas. In this area, where $N_p > 1$, the development of the ghost column deeply alters flow topology, and the isovorticity pattern around the sphere is now saddled-shaped owing to MHD-induced tendency toward two dimensionality. The value of the electromagnetic drag coefficient now clearly overcomes the purely hydrodynamic one. If we extrapolate correlation (28) to higher N_p regions, the matching with Hunt and Ludford's theory limit (green plane) is highly satisfactory. As previously highlighted, in this area, a scaling law relates $C_{d,em}$ with N_p^p/Re_p^q , and both p and q approach 0.5 in the limit $N_p \gg 1$.

Obviously, correlation (28) should be benchmarked (and refined) by other numerical or experimental results for the same typical geometry. The part of area III for which $\text{Re}_p, N_p \gg 1$ is expected to be particularly challenging: For instance, for $\text{Re}_p = 130$, the Hartmann number Ha should reach a value of several thousands, rising such numerical issues as proper meshing of the Hartmann layers at the surface of the sphere and at duct walls. Meanwhile, correlation (28) is a first step toward a generalized scaling law for confined MHD flows around spheres.

IV. CONCLUSIONS AND OUTLOOK

A permanent MHD channel flow past a sphere has been successfully investigated, based on a 3-D numerical approach, taking properly confinement effects into account, when the magnetic field is transversally applied. A fair agreement is found with existing literature allowing for asymptotic benchmark ($\text{Ha} \rightarrow 0, \infty$). The joint presence of side walls and an obstacle like a sphere is crucial, essentially because it generates strong topological changes due to the development of Hartmann layers. As anticipated from Ref. [22], one demonstrates in the present paper that the symmetry breakup generated by the presence of a spherelike obstacle causes a strong interaction between the sphere and the channel walls by way of the electric circuit, which may significantly alter flow patterns as well as flow coefficients. More particularly, a first numerical evidence of the gradual emergence of a Hunt's wake at the location of the sphere is made evident for a sufficiently large particle Stuart number. Owing to MHD-induced tendency to two dimensionality, the isovorticity pattern around the sphere is found to switch from a wing-shaped to a saddle-shaped pattern for a growing transverse magnetic field. Other MHD working conditions are simulated and some original correlations for the wake length and drag coefficient with respect to MHD flow coefficients are drawn up. An original scaling law highlighting the significant influence of an outer transverse magnetic field on the transition between different MHD flow regimes is finally proposed.

It must be pointed out that present results could be extended by scrutinizing other values of the following parameters: the blockage ratio λ and other Re_p, N_p pairs. As previously said, the regimes linked to higher values of Re_p, N_p should be interesting (possible arising of Roberts singularities [47]) but quite challenging considering CPU costs, meshing issues risen by the thinness of the Hartmann layers, and the need for simulating the unsteady behavior of the sphere wake. The nature of the boundary condition at the surface of the sphere also could reveal to be an insightful topic for future studies on bubble MHD flow. The electrical activation of the Hartmann layers at the surface of the sphere, in link with the boundary condition implemented at its surface, should dramatically affect the MHD flow topology. A “true” boundary condition spanning between slip and no-slip BCs [42,48–50] as well as a proper numerical implementation of the full jump momentum balance at the liquid/gas interface (following, e.g., the approach of Reusken and Zhang [51]) should be considered as a future step toward the description of MHD bubble flows.

ACKNOWLEDGMENTS

The authors wish to thank Prof. A. Pothérat for allowing them to use two images contained in the thesis of Dr. V. Dousset [Figs. 5 and 6(a)]. They also wish to acknowledge Dr. W. Haverkoort and Dr. T. Peeters for giving them the opportunity to use the image displayed in Fig. 6(b). Cambridge University Press is acknowledged for having granted to the authors the nonexclusive permission, free of charge, to use the material displayed in Fig. 4. The authors are also grateful to the French Ministry for Higher Education and Research for the Ph.D. fellowship received by Dr. Jules Delacroix. Finally, the authors would also thank one referee for comments which contributed to a significant improvement of the quality of the paper. The laboratory SIMAP is part of the LabEx Tec 21 (Investissements d’Avenir, Grant Agreement No. ANR-11-LABX-0030).

APPENDIX A: STREAMWISE OR TRANSVERSE MAGNETIC FIELD?

Let us highlight an issue of particular interest in view of magnifying the interplay between bulk MHD and the spherical inclusion, related to the respective orientations of the velocity field *ad infinitum* and of the outer dc field. Let us determine whether a *streamwise* or a *transverse* configuration seems more insightful by considering the case of an insulating sphere (rigid bubble) rising freely in an unbounded medium, and let us investigate here the streamwise configuration, where the velocity and the outer magnetic field are aligned (along the \vec{e}_x direction) far from the inclusion. The governing MHD equations provide particularly insightful information.

The spherical system of coordinates attached to the sphere, as defined in Fig. 8, is used, and a potential formulation of the MHD problem is selected. After an appropriate scaling (dimensionless quantities being superscripted \star), the potential formulation leads to the following MHD equation [5] for the electric potential ϕ^\star :

$$\Delta^\star \phi^\star = \text{div}^\star(\vec{v}^\star \times \vec{e}_x).$$

Let us develop further this equation by projecting \vec{e}_x on the spherical frame $(\vec{e}_r, \vec{e}_\theta, \vec{e}_\varphi)$: Classically, $\vec{e}_x = \sin(\theta)\vec{e}_r + \cos(\theta)\vec{e}_\theta$, and here $\vec{v}^\star = v_r^\star(r^\star, \theta)\vec{e}_r + v_\theta(r^\star, \theta)\vec{e}_\theta$ for symmetry reasons. Consequently, the vector $\vec{v}^\star \times \vec{e}_x$ is oriented along the single \vec{e}_φ component, but depends on r and θ alone. Its divergence is consequently zero, resulting in

$$\Delta^\star \phi^\star = 0. \tag{A1}$$

Now, with the outer field being oriented along the \vec{e}_x direction, Ohm’s law delivers the following expression for the electric current densities \vec{j}^\star [5]:

$$\vec{j}^\star = -\overrightarrow{\text{grad}}(\phi^\star) + \vec{v}^\star \times \vec{e}_x = -\frac{\partial \phi^\star}{\partial r^\star} \vec{e}_r - \frac{1}{r^\star} \frac{\partial \phi^\star}{\partial \theta} \vec{e}_\theta + [v_r^\star \sin(\theta) - v_\theta^\star \cos(\theta)] \vec{e}_\varphi, \tag{A2}$$

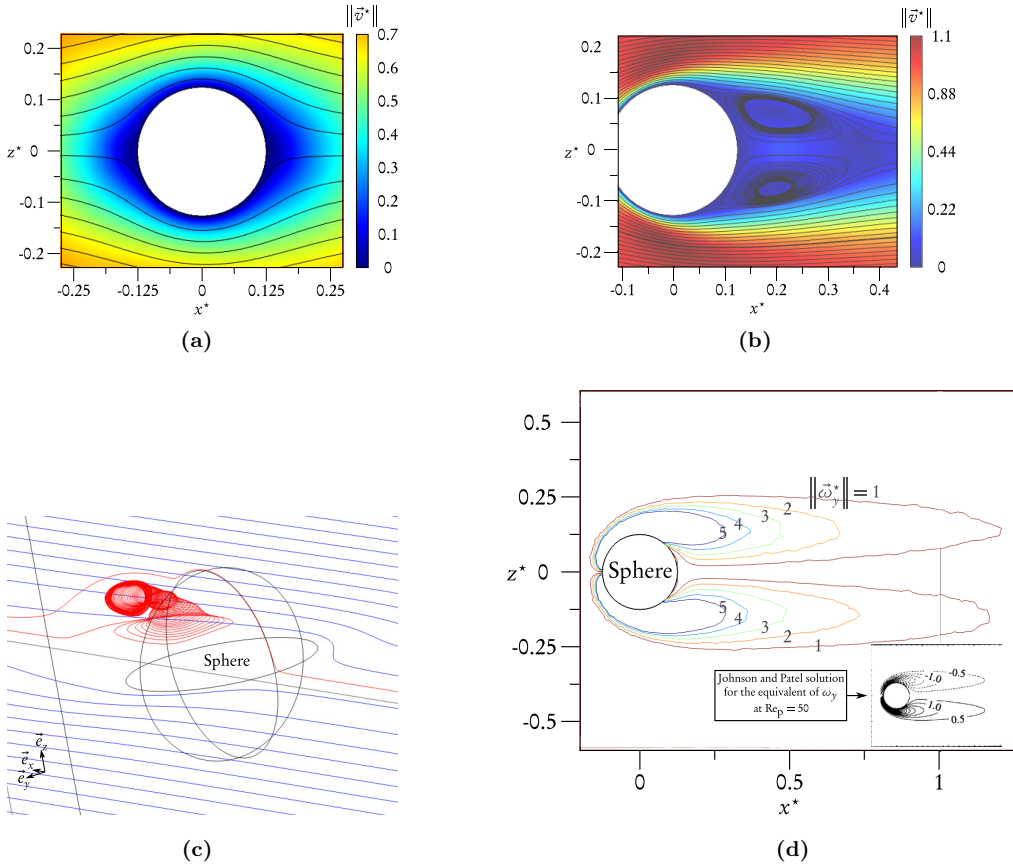


FIG. 18. Hydrodynamic flow patterns around the sphere. (a) Norm (color scale) and streamlines of the velocity field \vec{v}^* in (xz) , for $Re_p = 1.1$; (b) norm (color scale) and streamlines of the velocity field \vec{v}^* in (xz) , for $Re_p = 125.9$; (c) \vec{v}^* streamlines at $Re_p = 125.9$: recirculation region (red) and (xy) (blue); (d) $\|\omega_y^*\|$ contours in (xz) , for $Re_p = 52.6$. Inset: Equivalent of (dimensional) vorticity ω_y contours at $Re_p = 52.9$, from Ref. [53].

where the $\vec{\text{grad}}(\phi^*)$ and $\vec{v}^* \times \vec{e}_x$ terms are denominated the Coulomb and Lorentz parts of the electric current densities, respectively.

As such, Eq. (A1) does not bring any source term due to velocity into play. Moreover, the electric current densities, given in Eq. (A2), do not depend on velocity as far as the in-plane components are concerned, while the out-of-plane component is purely electromotive. As such, only a passive interplay between the Coulomb and Lorentz part is expected, with no need for the electrical activation of the Hartmann layers along the sphere, which would not deeply alter the core-flow topology.³

In the light of these remarks, we shall focus on the transverse configuration in this paper, with $\vec{B}_0 = B_0 \vec{e}_z$. However, this choice has a major drawback: The axisymmetry of the problem is broken, which considerably compromises an analytical approach to the problem. It is also worth noting that the presence of duct walls also leads to symmetry breakup. For all these reasons, a numerical approach is favored in this paper (see Sec. II).

³Except in the case where the wake becomes unstable; see, e.g., a very recent paper by Pan *et al.* [52] in the case of slip conditions applied at the channel walls.

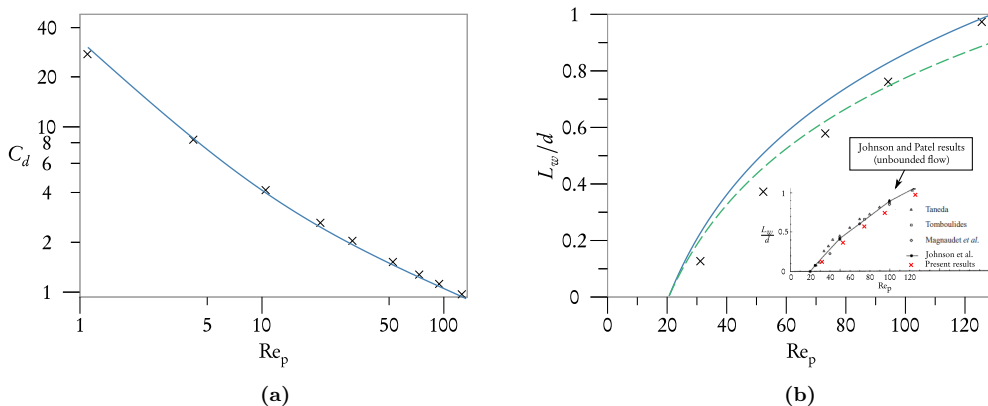


FIG. 19. Evolution of flow coefficients with respect to Re_p . (a) Drag coefficient with respect to various Re_p values. Line, correlation (12); symbols, present results; (b) wake length relative to sphere diameter for various Re_p values. Solid line, correlation (10); dashed line, $0.9 \times (10)$; cross symbols, present results. Inset: different wake length results exposed in Ref. [53] compared to present results.

APPENDIX B: BENCHMARK WITH THE PURELY HYDRODYNAMIC CASE ($Ha = 0$)

This Appendix focuses on the benchmarking asymptotic study relative to the purely hydrodynamic case $Ha = 0$.

1. Flow patterns

The hydrodynamic flow patterns are in satisfying agreement with the different observations made in Sec. I C 1. When Re_p is small, the Stokes flow patterns are recovered in Fig. 18(a). When Re_p is large enough, the steady wake regime is observed in Fig. 18(b) with the arising of a counter-clockwise vortex pair (also referred to as twin vortices or vortex bubble in the literature; see, e.g., Ref. [54]). The flow acceleration due to confinement is seen in the magnitude of the velocity field, which reaches higher values than at the inlet, in the regions between the top (respectively the bottom) of the sphere and the top (respectively bottom) duct wall. Flow separation and recirculating areas are noticeable in the vicinity of the sphere, as magnified in Fig. 18(c). Finally, the vorticity contours ω_y^* in the plane (xz) [see Fig. 18(d)] are in qualitative agreement with those found, e.g., in Ref. [53] at the same value of Re_p .⁴ The underlying vortical structure of the wake explains the toroidal vortex observed in the streamline patterns and the emergence of the steady recirculating areas.

2. Flow coefficients

Once again, the agreement between numerical results and the predictions stemming from the state of the art is relatively satisfying. Concerning the drag coefficient C_d [see Fig. 19(a)], the evolution with respect to Re_p follows the one predicted by Eq. (12), and the mean error lies within 2%. With respect to the wake length [see Fig. 19(b)], the results seem less satisfying when compared directly with Eq. (10). The agreement is far better when considering 10% lower values for the latter, taking account of the blockage ratio, except for Re_p numbers close to the creeping flow/steady wake transition. If now we consider other results exposed, e.g., in Ref. [53] [inset of Fig. 19(b)], the present results seem quite relevant. The other results indeed correspond to unbounded flow studies, where the ratio L_w/d is consequently larger than for confined layouts, as is the case in this study. As

⁴The authors do not explicitly define a dimensionless vorticity, preventing us from concluding on the quantitative agreement.

expected, this feature is systematically found in the inset of Fig. 19(b) (the discrepancy lying within 10%, as previously said in link with the confinement). Consequently, the hydrodynamic benchmark makes us reasonably confident about the validity of the numerical simulations.

APPENDIX C: NUMERICAL PRECISION OF THE CODE

In order to give an estimate of the numerical precision, two different tests are performed. First, the mesh is significantly refined with the standard geometry: from 9×10^5 (standard mesh) up to 1.4×10^6 elements (heavy mesh). Second, the outflow conditions are modified in order to check whether the $15d$ distance downstream from the sphere constitutes a sufficient “buffer” region or not. This distance is extended up to $22d$. Three cutting lines are defined:

(1) A first one, along the main x axis, spanning from the rear of the sphere to $x = 10d$ within the $z = 0$ plane,

(2) a second one, along the transverse direction \vec{e}_y , spanning between the two side walls within the (yz) plane at $x = 7.5d$, and

(3) a last one, along the direction of the magnetic field \vec{e}_z , spanning between the bottom and top duct walls, within the (yz) plane at $x = 7.5d$.

For each layout (standard mesh, heavy mesh, and longer duct), the y component of the electric current density and the x component of the velocity along the three cutting lines have been compared for various Reynolds numbers at a given Ha value ($Ha = 10$). As all the curves being perfectly superimposed in each case, both the numerical precision of the code and the numerical implementation of the sphere MHD problem can be considered as secured.

-
- [1] A. H. A. Hamid, W. K. Hussam, and G. J. Sheard, Combining an obstacle and electrically driven vortices to enhance heat transfer in a quasi-two-dimensional mhd duct flow, *J. Fluid Mech.* **792**, 364 (2016).
 - [2] B. D. Plouffe and S. K. Murthy, Perspective on microfluidic cell separation: A solved problem? *Anal. Chem.* **86**, 11481 (2014).
 - [3] J. W. Haverkort and T. W. J. Peeters, Magnetohydrodynamic effects on insulating bubbles and inclusions in the continuous casting of steel, *Metall. Mater. Trans. B* **41**, 1240 (2010).
 - [4] S. Smolentsev, N. B. Morley, M. A. Abdou, and S. Malang, Dual-coolant lead-lithium (DCLL) blanket status and R&D needs, *Fusion Eng. Des.* **100**, 44 (2015).
 - [5] R. Moreau, *Magnetohydrodynamics* (Kluwer Academic, Dordrecht, the Netherlands, 1990), Chaps. 1, 4, 5, pp. 1–31, 110–150, 179–189.
 - [6] A. H. A. Hamid, W. K. Hussam, and G. J. Sheard, Heat transfer augmentation of a quasi-two-dimensional MHD duct flow via electrically driven vortices, *Numer. Heat Transfer, Part A* **70**, 847 (2016).
 - [7] W. K. Hussam, A. H. A. Hamid, Z. Y. Ng, and G. J. Sheard, Effect of vortex promoter shape on heat transfer in MHD duct flow with axial magnetic field, *Int. J. Therm. Sci.* **134**, 453 (2018).
 - [8] J. H. Pendergrass, L. A. Booth, D. R. Peterson, and S. A. W. Gerstl, The lithium boiler - A 1500 to 2000 K fusion reactor blanket concept for process heat and/or electric power generation, in *14th Intersociety Energy Conversion Engineering Conference*, Vol. 2 (American Chemical Society, Washington, D.C., 1979), pp. 1597–1607.
 - [9] J. D. Bender and M. A. Hoffman, A two-phase flow cooling concept for fusion reactor blankets, Lawrence Livermore National Laboratory, Livermore, LLNL Report UCRL-78892, 1977 (unpublished).
 - [10] M. Takahashi, A. Inoue, M. Aritomi, and M. Matsuzaki, Studies on magnetohydrodynamic flow characteristics and heat transfer of liquid metal two-phase flow cooling systems for a magnetically confined fusion reactor, *Fusion Eng. Des.* **27**, 663 (1995).
 - [11] C. Zhang, S. Eckert, and G. Gerbeth, The flow structure of a bubble-driven liquid-metal jet in a horizontal magnetic field, *J. Fluid Mech.* **575**, 57 (2007).

- [12] X. Miao, D. Lucas, Z. Ren, S. Eckert, and G. Gerbeth, Numerical modeling of bubble-driven liquid metal flows with external static magnetic field, *Int. J. Multiphas. Flow* **48**, 32 (2013).
- [13] S. Eckert, G. Gerbeth, and O. Lielausis, The behaviour of gas bubbles in a turbulent liquid metal magnetohydrodynamic flow. Part II: Magnetic field influence on the slip ratio, *Int. J. Multiphase Flow* **26**, 67 (2000).
- [14] K. Takatani, Mathematical modeling of incompressible MHD flows with free surface, *ISIJ Int.* **47**, 545 (2007).
- [15] J. Zhang and M.-J. Ni, Direct simulation of single bubble motion under vertical magnetic field: Paths and wakes, *Phys. Fluids* **26**, 102102 (2014).
- [16] J. Zhang, M.-J. Ni, and R. Moreau, Rising motion of a single bubble through a liquid metal in the presence of a horizontal magnetic field, *Phys. Fluids* **28**, 032101 (2016).
- [17] K. Jin, P. Kumar, S. P. Vanka, and B. G. Thomas, Rise of an argon bubble in liquid steel in the presence of a transverse magnetic field, *Phys. Fluids* **28**, 093301 (2016).
- [18] C. Zhang, S. Eckert, and G. Gerbeth, Experimental study of single bubble motion in a liquid metal column exposed to a dc magnetic field, *Int. J. Multiphase Flow* **31**, 824 (2005).
- [19] J. Sommeria and R. Moreau, Why, how, and when MHD turbulence becomes two-dimensional, *J. Fluid Mech.* **118**, 507 (1982).
- [20] M. Frank, L. Barleon, and U. Müller, Visual analysis of two-dimensional magnetohydrodynamics, *Phys. Fluids* **13**, 2287 (2001).
- [21] B. Mück, C. Günther, U. Müller, and L. Bühler, Three-dimensional MHD flows in rectangular ducts with internal obstacles, *J. Fluid Mech.* **418**, 265 (2000).
- [22] J. C. R. Hunt and G. S. S. Ludford, Three-dimensional MHD duct flows with strong transverse magnetic field. Part 1. Obstacles in a constant area channel, *J. Fluid Mech.* **33**, 693 (1968).
- [23] J. W. Haverkort and T. W. J. Peeters, Magnetohydrodynamics of insulating spheres, *Magnetohydrodynamics* **45**, 111 (2009).
- [24] V. Dousset, Numerical simulations of MHD flows past obstacles in a duct under externally applied magnetic field, Ph.D. thesis, Coventry University, Coventry, UK, 2009 (unpublished).
- [25] R. Clift, J. R. Grace, and M. E. Weber, *Bubbles, Drops, and Particles* (Academic Press, New York, 1978), Chaps. 2 and 3, pp. 16–68.
- [26] A. Maheshwari, R. P. Chhabra, and G. Biswas, Effect of blockage on drag and heat transfer from a single sphere an an in-line array of three spheres, *Powder Technol.* **168**, 74 (2006).
- [27] R. M. Wham, O. A. Basaran, and C. H. Byers, Wall effects on flow past solid spheres at finite Reynolds number, *Ind. Eng. Chem. Res.* **35**, 864 (1996).
- [28] T. V. S. Sekhar, T. V. R. Ravikumar, and H. Kumar, MHD flow past a sphere at low and moderate Reynolds numbers, *Comput. Mech.* **31**, 437 (2003).
- [29] V. Dousset and A. Pothérat, Characterization of the flow past a truncated square cylinder in a duct under a spanwise magnetic field, *J. Fluid Mech.* **691**, 341 (2012).
- [30] J. C. R. Hunt, Bluff body drag in a strong transverse magnetic field, *Magnetohydrodynamics* **6**, 35 (1970).
- [31] J. Reitz and L. Foldy, The force on a sphere moving through a conducting fluid in the presence of a magnetic field, *J. Fluid Mech.* **11**, 133 (1961).
- [32] A. Pothérat, J. Sommeria, and R. Moreau, Effective boundary conditions for magnetohydrodynamic flows with thin Hartmann layers, *Phys. Fluids* **14**, 403 (2002).
- [33] J. A. Shercliff, Steady motion of conducting fluids in pipes under transverse magnetic fields, *J. Fluid Mech.* **49**, 136 (1953).
- [34] O. Andreev, Y. Kolesnikov, and A. Thess, Visualization of the Ludford column, *J. Fluid Mech.* **721**, 438 (2013).
- [35] G. Branover, N. Slyusarev, and A. Tsinober, Drag of a sphere in a magnetohydrodynamic flow, *Magnetohydrodynamics* **2**, 149 (1966).
- [36] N. T. Baker, A. Pothérat, L. Davoust, F. Debray, and R. Klein, Controlling the dimensionality of low-Rm MHD turbulence experimentally, *Exp. Fluids* **58**, 79 (2017).
- [37] M. Bertherat, T. Odievre, M. Allibert, and P. Le Brun, A radiosopic technique to observe bubbles in liquid aluminium, *Light Met.* **3**, 861 (2002).

- [38] J. A. Shercliff, *A Textbook of Magnetohydrodynamics* (Pergamon Press, Oxford, 1965), Chap. 2, pp. 9–30.
- [39] Y. Plevachuk, V. Sklyarchuk, S. Eckert, G. Gerbeth, and R. Novakovic, Thermophysical properties of the liquid Ga-In-Sn eutectic Alloy, *J. Chem. Eng. Data* **59**, 757 (2014).
- [40] T. Liu, P. Sen, and C.-J. Kim, Characterization of nontoxic liquid-metal alloy galinstan for applications in microdevices, *J. Microelectromech. S.* **21**, 443 (2012).
- [41] T. E. Tezduyar and R. Shih, Numerical experiments on downstream boundary of flow past cylinder, *J. Eng. Mech.* **117**, 854 (1991).
- [42] J. Delacroix and L. Davoust, On the role of surface rheology in a magnetohydrodynamic swirling flow, *Phys. Fluids* **27**, 062104 (2015).
- [43] S. V. Patankar, *Numerical Heat Transfer and Fluid Flow* (Hemisphere, Washington, DC, 1980).
- [44] D. W. Marquardt, An algorithm for least-squares estimation of nonlinear parameters, *J. Soc. Ind. Appl. Math.* **11**, 431 (1963).
- [45] Y. Saad and M. H. Schultz, GMRES: A generalized minimal residual algorithm for solving nonsymmetric linear systems, *SIAM J. Sci. Stat. Comput.* **7**, 856 (1986).
- [46] P. R. Amestoy, I. S. Duff, J.-Y. L'Excellent, and J. Koster, A fully asynchronous multifrontal solver using distributed dynamic scheduling, *SIAM J. Matrix Anal. Appl.* **23**, 15 (2001).
- [47] P. H. Roberts, Singularities of Hartmann layers, *Proc. R. Soc. London A* **300**, 94 (1967).
- [48] C. Zhang, V. Shatrov, J. Priede, S. Eckert, and G. Gerbeth, Intermittent behavior caused by surface oxidation in a liquid metal flow driven by a rotating magnetic field, *Metall. Mater. Trans. B* **42**, 1188 (2011).
- [49] J. Delacroix and L. Davoust, Electrical activity of the Hartmann layers relative to surface viscous shearing in an annular magnetohydrodynamic flow, *Phys. Fluids* **26**, 037102 (2014).
- [50] J. Delacroix, L. Davoust, and K. Patouillet, Low Rm magnetohydrodynamics as a means of measuring the surface shear viscosity of a liquid metal: A first attempt on galinstan, *Rev. Sci. Instrum.* **89**, 015103 (2018).
- [51] A. Reusken and Y. Zhang, Numerical simulation of incompressible two-phase flows with a Boussinesq-Scriven interface stress tensor, *Int. J. Numer. Meth. Fluids* **73**, 1042 (2013).
- [52] J.-H. Pan, N.-M. Zhang, and M.-J. Ni, The wake structure and transition process of a flow past a sphere affected by a streamwise magnetic field, *J. Fluid Mech.* **842**, 248 (2018).
- [53] T. A. Johnson and V. C. Patel, Flow past a sphere up to a Reynolds number of 300, *J. Fluid Mech.* **378**, 19 (1999).
- [54] M. Sahin and R. G. Owens, A numerical investigation of wall effects up to high blockage ratios on two-dimensional flow past a confined circular cylinder, *Phys. Fluids* **16**, 1305 (2004).